Stable 3D extended finite elements with higher order enrichment for accurate non planar fracture

Konstantinos Agathos [a], Eleni Chatzi [b] and Stéphane P. A. Bordas [c,d]

[a] *Institute of Structural Analysis and Dynamics of Structures, Department of Civil Engineering, Aristotle University Thessaloniki, Panepistimioupolis Mail Stop 502, 54124 Thessaloniki, Greece*

[b] *Institute of Structural Engineering, ETH Zürich, Stefano-Franscini-Platz 5, CH-8093 Zürich, Switzerland*

[c] *Research Unit in Engineering Science, Luxembourg University, 6 rue Richard Coudenhove-Kalergi, L-1359 Luxembourg, Luxembourg*

[d] *Institute of Theoretical, Applied and Computational Mechanics, Cardiff University, Cardiff CF24 3AA, U.K.*

Abstract

We present an extended finite element method (XFEM) for 3D non-planar linear elastic fracture. The new approach not only provides optimal convergence using geometrical enrichment but also enables to contain the increase in conditioning number characteristic of enriched finite element formulations: the number of iterations to convergence of the conjugate gradient solver scales similarly to and converges faster than the topologically-enriched version of the standard XFEM. This has two advantages: (1) the residual can be driven to zero to machine precision for at least 50% fewer iterations than the standard version of XFEM; (2) additional enrichment functions can be added without significant deterioration of the conditioning. Numerical examples also show that our new approach is up to 40% more accurate in terms of stress intensity factors, than the standard XFEM.

Key words: XFEM, geometrical enrichment, weight function blending, dof gathering, conditioning

* Corresponding author: Stéphane P. A. Bordas (E-mail:stephane.bordas@alum.northwestern.edu)

1 Introduction

Following the introduction of the partition of unity method (PUM) [1] a number of enriched finite element methods have appeared which allow the infusion of *a priori* knowledge on the solution within the approximation scheme, thereby enabling the numerical method to reproduce essential features of the solution. In the context of non-planar fracture, we propose in this paper a new approach which addresses, at the same time, two of the major difficulties which have plagued these enriched finite element methods: uncontrolled increase of the condition number of the system matrix for large enrichment radii (necessary for optimal convergence) or/and large numbers of enrichment functions ; and the blending between different partitions of unity at the interface between the enriched and standard regions of the computational domain.

We place ourselves in the context of the extended finite element method (XFEM) which appeared in 1999 by Ted Belytschko's group [2,3] and has been used since then to simulate, among a number of other phenomena involving free boundaries, crack propagation. Through discontinuous and near-tip enrichment respectively, the XFEM eliminates the need for the mesh to conform to the crack faces and reduces the density of the mesh around the crack front [4,5,6]. The first industrial damage tolerance assessment simulations with XFEM were reported in [7,8] and [9] and the method is today in use industrially, e.g. within the commercial code Morfeo Crack [10,11].

The academic and industrial success of the XFEM is likely attributable to a large body of research which has been focusing on addressing some of the shortcomings associated with the 1999 version of the method. We review here briefly the work related to lack of optimal convergence, blending and conditioning, mainly in the framework of linear elastic fracture mechanics.

In [12] and [13,14], the lack of optimal convergence was observed when only one element is enriched and as a remedy the enrichment of elements in a fixed area (independent of the mesh size) around the crack tip/front (geometrical enrichment) [13,15] was proposed. This geometrical enrichment approach does restore optimal convergence which is lost when only one element is enriched (topological enrichment), where the part played by the enrichment vanishes with the element size. However, enriching an increasing number of nodes, those which fall within the enrichment zone, as the mesh is refined also creates more propensity for the system matrix to be ill-conditioned.

Conditioning issues can be solved using special preconditioners [14] and [16]; the degree of freedom (dof) gathering [13,17] technique, which aims at reducing the variability of the enriched fields in the enrichment zone. Alternatively, the so-called "Stable" version of the enrichment method may be used, obtained by

subtracting the projection of the enrichment functions onto the finite element basis [18].

Blending problems between the enriched and the standard part of the approximation can also cause lack of optimal convergence or decreased accuracy depending on the type of enrichment functions used. Several approaches have been proposed from 2003 to as recently as 2011 [19,20,21,22,23,24].

Numerical integration is also crucial to achieving optimal convergence and increased accuracy. In particular, it is important to minimize numerical integration errors which are mostly associated with the singular nature of the tip enrichment functions. Several integration schemes can be found in the literature most of which employ element partitioning either solely [3,24] or in conjunction to special mappings [13,14,25,26,27] while others attempt to completely avoid element partitioning [28,23,29,30,31]. Methods have also been introduced which attempt to minimize the number of Gauss points resulting from element partitioning and singular mappings [32].

Concerning the particular application of enriched finite elements to fracture mechanics, several extensions of these methods have been proposed to increase the accuracy of the quantities of interest, i.e. the stress intensity factors. For example, the addition of higher order terms in the near tip asymptotic fields allows the direct evaluation of stress intensity factors (SIFs) [33,34,35]. A second approach is the use of Irwin's integral [36,37,38]. Finally, specially tailored error estimators were proposed in a series of papers starting in 2006 for the generalized finite element method (GFEM) [39] and in 2007 for XFEM [40]. Error estimators [41,42,43] significantly improve the accuracy of the primal and dual quantities as well as that of the stress intensity factors, or other quantities of engineering interest [44,45,46].

The development of such error estimators was motivated by the oscillatory and inaccurate nature of stress intensity factors obtained from XFE solutions in industrial applications [7]. Since then, significant work has been devoted (completely or partially) to the evaluation of stress intensity factors using the interaction integral method within an XFE framework [3,4,5,47,48].

Two of the most important weaknesses mentioned above, which are often correlated, are the lack of optimal convergence and the blending problems. For the former, an attractive solution is the use geometrical enrichment [13,14,15] in conjunction to dof gathering [13] which also solves the conditioning problems and greatly reduces the number of enriched dofs. This method, which has been recently extended to 3D [17], is typically combined with a blending correction technique in order to provide improved accuracy.

As far as blending is concerned, one of the most successful solutions within the 2D XFEM framework is the corrected XFEM [20] which has been extended and

combined to dof gathering in the work of Ventura et al. [23]. One drawback of the corrected XFEM is the fact that, when combined with the standard branch enrichment functions, it introduces a singularity. The latter is dealt with by dropping the appropriate equations from the resulting system. Since in 3D the selection of those equations is not straightforward, Loehnert et al. [24] introduced an alternative procedure which consists of employing only three of the four branch enrichment functions.

In the present work, we investigate the combination of the enrichment scheme introduced in [17] (an extension of dof gathering to 3D) to the corrected XFEM approach [20] and its extensions [23]. This combination provides a means of extending the corrected XFEM to 3D without decreasing the number of enrichment functions (as in [24]) and, in addition improves the performance of the global enrichment approach and simplifies its implementation.

As a result of the improved conditioning of the resulting method, the possibility is given, for the first time in 3D XFEM, to study the effect of the addition of higher order enrichment functions on the overall accuracy of the method. With existing approaches, higher order enrichment functions can only be used with topological enrichment since their combination with geometrical enrichment leads to uncontrolled condition numbers for the system matrix. We also present a new simple element partitioning technique, associated with the new enrichment scheme used and present a novel, accurate and robust SIF evaluation procedure.

We verify the method on a range of 3D problems also involving non-planar cracks.

2 Problem Statement

Consider the problem of a cracked domain Ω bounded by the boundary Γ consisting of the parts Γ_0, Γ_u where displacements $\bar{u}$ are imposed as Dirichlet boundary conditions, Γ_t where the surface tractions $\bar{t}$ are applied as Neumann conditions and the crack surface Γ_c where $\Gamma = \Gamma_0 \cup \Gamma_u \cup \Gamma_t \cup \Gamma_c$ and $\Gamma_c = \Gamma_c^t \cup \Gamma_c^0$ as depicted in Figure 1. It should be noted that surface tractions $\bar{t}_c$ are also applied along a part of the crack surface (Γ_c^t).

The weak form of the equilibrium equations is formulated as:

Find a kinematically admissible displacement field $\boldsymbol{u} \in \mathcal{U}$ such that $\forall \boldsymbol{v} \in \mathcal{V}^0$

$$\int_\Omega \boldsymbol{\epsilon}(\boldsymbol{u}) : \boldsymbol{D} : \boldsymbol{\epsilon}(\boldsymbol{v}) \; d\Omega = \int_\Omega \boldsymbol{b} \cdot \boldsymbol{v} \; d\Omega + \int_{\Gamma_t} \bar{\boldsymbol{t}} \cdot \boldsymbol{v} \; d\Gamma + \int_{\Gamma_c^t} \bar{\boldsymbol{t}}_c \cdot \boldsymbol{v} \; d\Gamma_c^t \qquad (1)$$

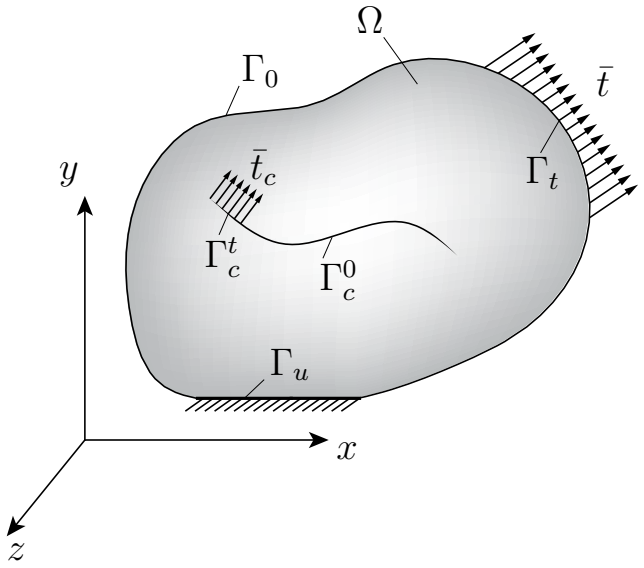

Fig. 1. Cracked Body and boundary conditions.

where :

$$\mathcal{U} = \left\{ \boldsymbol{u} | \boldsymbol{u} \in \left(H^1 \left(\Omega \right) \right)^3, \boldsymbol{u} = \bar{\boldsymbol{u}} \text{ on } \Gamma_u \right\} \tag{2}$$

and

$$\mathcal{V} = \left\{ \boldsymbol{v} | \boldsymbol{v} \in \left(H^1 \left(\Omega \right) \right)^3, \boldsymbol{v} = \boldsymbol{0} \text{ on } \Gamma_u \right\} \tag{3}$$

Functions of $H^1(\Omega)$ are implicitly discontinuous along the crack surface.

In the above, $\boldsymbol{\epsilon}$ is the small strain field, $\boldsymbol{D}$ is the elasticity tensor and $\boldsymbol{b}$ is the applied body force per unit volume.

3 The proposed method

As mentioned in Section 1, the corrected XFEM approach [20] and its extensions [23] will be employed in this work in order to eliminate blending errors. In this method, the enrichment functions are weighted by a function which assumes a value of zero for standard elements, a value of unity for elements with all of their nodes being enriched and varies continuously for elements consisting of both enriched and standard nodes (blending elements). The above result is achieved by using as a weight function, for every element, the sum of the shape functions corresponding to enriched nodes. In addition, all nodes

of blending elements are enriched so that the partition of unity property is preserved in those elements as well. Finally, shifted enrichment functions are typically used in order to retain the Kronecker-δ property in enriched elements.

The work of Ventura et al. [23] extended the above concepts by using more general weight functions, which spread along several layers of elements. The method was also applied to cases where all enriched degrees of freedom are constrained to be equal which, for crack problems, is equivalent to using the degree of freedom gathering technique [13].

The above methods provide a means of eliminating blending errors as well as obtaining optimal convergence without conditioning problems. However, the extension of the corrected XFEM to 3D requires the decrease of the number of tip enrichment functions [24]. Moreover, the extension of the method of Ventura et al. to 3D would require the extension of dof gathering which until recently was not possible. In this work, those problems are solved by combining the enrichment scheme presented in our previous work [17] with a three-dimensional extension of the blending and shifting techniques presented in the work of Ventura et al. [23].

3.1 Crack representation

As in [17] the method introduced herein can be used in conjunction to any of the available crack representation methods, for instance level sets [5,6,49], vector level sets [50] or a hybrid explicit implicit representation [51].

In the remainder of this work, a level set representation [5,6,49] will be used and the level set functions will be denoted as ϕ and ψ. For an arbitrary point $\mathbf{x}$ in the domain:

- ϕ is the signed distance from the crack surface defined as:

$$\phi(\mathbf{x}) = \min_{\bar{\mathbf{x}} \in \Gamma_c} \|\mathbf{x} - \bar{\mathbf{x}}\| \operatorname{sign}\left(\mathbf{n}^+ \cdot (\mathbf{x} - \bar{\mathbf{x}})\right) \tag{4}$$

  where $\mathbf{n}^+$ is the outward normal to the crack surface and $\operatorname{sign}()$ is the sign function.
- ψ is a signed distance function such that $\nabla\phi \cdot \nabla\psi = 0$ and $\phi(\mathbf{x}) = 0$ and $\psi(\mathbf{x}) = 0$ defines the crack front.

The polar coordinates used for the definition of the enrichment functions are defined as [5,6,49]:

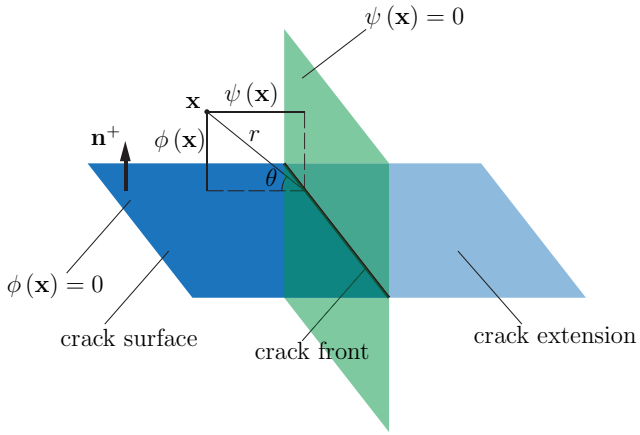

Fig. 2. Level set functions and polar coordinate system for a planar crack.

$$r = \sqrt{\phi^2 + \psi^2}, \qquad \theta = \arctan\left(\frac{\phi}{\psi}\right) \tag{5}$$

Both the definition of the level set functions and the polar coordinate system are illustrated in Figure 2 for a simple planar crack.

3.2 Definition of the front elements

A global tip enrichment strategy [17] is adopted in this work, which introduces a mesh of superimposed elements whose shape functions provide a basis using which the tip enrichment functions can be weighted. This basis should satisfy the partition of unity property and, in addition, provide spatial variation along the direction of the crack front while inhibiting variation in the plane normal to the crack front. The last requirement is introduced in order to avoid conditioning problems.

Some concepts similar to the superimposed mesh used in this work, are the analytical patch used in the work of Langlois et al.[52] and the s-finite element method [53]. The difference from both methods however is that in the present method the superimposed mesh is only used for weighting the singular enrichment functions.

The superimposed mesh consists of a set of points and linear univariate elements along the crack front, as depicted in Figure 3. Boundaries of those elements are defined by planes passing through the front nodes. The direction of those planes is defined according to the crack geometry.

In order to facilitate the interactions of the superimposed mesh, defined by front elements, with the FE mesh an additional parameter similar to the level

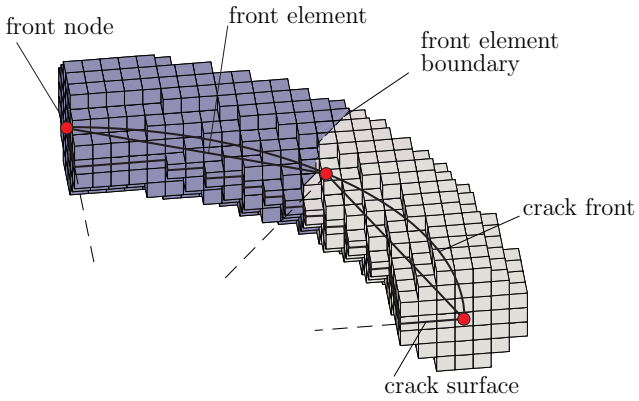

Fig. 3. Front elements, nodes and boundaries.

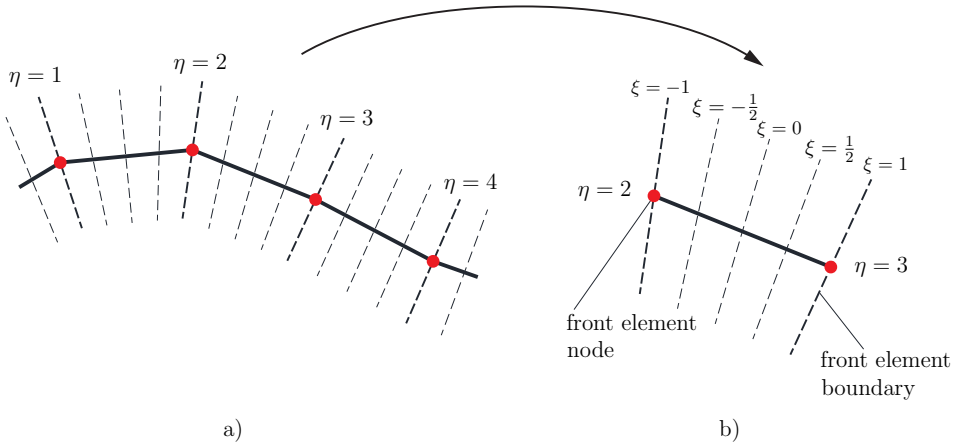

Fig. 4. a) Iso lines of the front parameter η. b) Local coordinate ξ of the front elements.

sets is defined which varies along the direction of the crack front. This parameter assumes integer values on the front nodes and the planes defined by front nodes and varies linearly in-between (Figure 4).

The local coordinates of the front elements are then defined in a similar manner to the front parameter as illustrated in Figure 4.

Linear 1D shape functions will be used for the front elements throughout this work:

$$\mathbf{N}^g(\xi) = \left[\frac{1-\xi}{2} \quad \frac{1+\xi}{2}\right] \tag{6}$$

where ξ is the local coordinate of the superimposed element.

The shape functions of the superimposed elements build a partition of unity, in addition their shape functions imply spatial variation only along one direction which is an approximation of the direction of the crack front. As a result these

can be employed for suitably weighting the tip enrichment functions.

3.3 Tip enrichment

It was shown in reference [17], and confirmed herein, that the proposed method results in improved conditioning of the resulting system matrices. This enables the addition of tip enrichment functions derived from higher order terms of the Williams expansion. Higher order terms have been used as enrichment functions in the 2D XFEM framework in several cotributions [33,34,13,35,36,37,38] mostly as a means of improving the accuracy of directly computed SIFs. In the present work, the effect of the higher order terms in the overall accuracy as well as in the conditioning of the method is studied.

Tip enrichment functions, including the higher order terms are defined as:

$$F_{ij}\left(\mathbf{x}\right) \equiv F_{ij}\left(r,\theta\right) = \left[F_{1j}\left(r,\theta\right), F_{2j}\left(r,\theta\right), \ldots\right]^{T} \tag{7}$$

where

$$\begin{aligned} F_{nj}\left(r,\theta\right) = \Bigg[& r^{(n-1/2)} \sin\left(n-\frac{1}{2}\right)\theta, r^{(n-1/2)} \cos\left(n-\frac{1}{2}\right)\theta, \\ & , r^{(n-1/2)} \sin\left(n-\frac{3}{2}\right)\theta \sin\theta, r^{(n-1/2)} \cos\left(n-\frac{3}{2}\right)\theta \sin\theta \Bigg] \end{aligned} \tag{8}$$

Parameters r and θ were defined in Subsection 3.1.

Those enrichment functions are derived from the higher order terms of the Williams expansion in a way identical to the one with which the standard enrichment functions are derived from the first term of the expansion [2]. A similar approach is adopted in some of the works mentioned above [13,36,37,38], while the rest [33,34,35] use the displacement expressions of the analytical solution directly as enrichment functions. This kind of enrichment has also been used in other works [27,54] which do not employ higher order terms and where it was found that it results in improved conditioning and a reduced number of enriched dofs. In Chevaugeon et al. [27] this enrichment type was referred to as 'vector enrichment' as opposed to 'scalar enrichment', which is more commonly used in XFEM implementations.

The reasoning behind the use of 'scalar enrichment' in this work is as follows: The scalar enrichment functions essentially form a basis able to represent the actual solution, and as a result they should be more general than the first

terms of the asymptotic expansion of the solution. In other words, by varying the coefficients of the four scalar tip enrichment functions, a variety of combinations can be achieved which also includes the first term of the asymptotic expansion. Since in our work the enrichment functions are not given the possibility to vary spatially, which somehow reduces the method's flexibility, the use of more general and thus flexible enrichment functions is desirable. This becomes more obvious when considering the fact that the method is aimed towards a wide variety of applications where the adopted underlying analytical solution is not essentially valid. Moreover, scalar enrichment, in contrast to vector enrichment, involves the same enrichment functions in each spatial dimension which simplifies the implementation of the method.

The enriched part of the displacement approximation for tip enriched elements, evaluated at $\mathbf{x} \in \Omega$, is written as a combination of the tip enrichment functions (Equation 7) with the global shape functions N_K^g associated with the superimposed elements (Equation 6):

$$\mathbf{u_t}\left(\mathbf{x}\right) = \sum_{K \in \mathcal{N}^s} N_K^g\left(\mathbf{x}\right) \sum_i \sum_j F_{ij}\left(\mathbf{x}\right) \mathbf{c}_{Kij} \tag{9}$$

where index K refers to nodes of the superimposed mesh and $\mathcal{N}^s$ is the set of superimposed nodes.

3.4 Jump enrichment

Jump enrichment functions are defined as:

$$H(\phi) = \begin{cases} 1 & \text{for } \phi > 0 \\ -1 & \text{for } \phi < 0 \end{cases} \tag{10}$$

The definition of ϕ was given in Subsection 3.1.

3.5 Weight function blending

In the present work two different definitions for the weight functions are used depending on the enrichment scheme used (topological or geometrical enrichment). In order to justify the use of those different definitions, some of the conclusions drawn from our previous work have to be taken into account. More specifically, it was observed that when spatial variation of the enrichment functions is not allowed and geometrical enrichment is used, jump enrichment is

also needed in tip enriched elements that contain the crack surface in order to account for displacement jumps caused by higher order terms of the near tip solution which can no longer be approximated by the tip enrichment functions since spatial variability is prohibited. When the enrichment radius contains only a couple of layers of elements the above situation does not cause any problems, however for larger enrichment radii the accuracy can deteriorate. As a result for the case where geometrical enrichment, with a large enrichment radius, a definition for the weight function is required which allows the enrichment of some nodes with both tip and jump enrichment functions.

Let N_T be the FE shape functions of the underlying mesh, the weight function for topological or geometrical enrichment with a small enrichment radius r_e assumes the form (Figure 5 a)):

$$\varphi(\mathbf{x}) = \sum_{T \in \mathcal{N}^{t1}} N_T(\mathbf{x}) \tag{11}$$

where $\mathcal{N}^{t1}$ is a set of nodes including all nodes belonging to elements which contain the crack front or nodes lying inside the enrichment radius. This definition is identical to the one proposed by Fries [20]. It should be noted that in this case only one layer of blending elements is employed (Figure 5 a)).

For geometrical enrichment, the weight function definition of Ventura et al. [23] will be used where the number of layers of blending elements can be controlled by appropriately defining the parameters involved. In more detail, once the enrichment radius r_e is given, an additional distance $r_i < r_e$ has to be specified so that the nodal values of the weight function φ_I take a value of unity inside the volume defined by r_i, a value of zero outside the volume defined by r_e and vary as a ramp function of order n in between:

$$\varphi_I = \begin{cases} 1, & g_I < 0 \\ (1 - g_I)^n, & 0 < g_I \leq 1 \\ 0, & g_I > 1 \end{cases} \tag{12}$$

where

$$g_I = \frac{r_I - r_i}{r_e - r_i} \tag{13}$$

and r_I are the nodal values of parameter r defined in Subsection 3.1. Parameter n will be given a value of unity so that the weight function varies linearly.

Weight function values are obtained from the nodal values through FE interpolation:

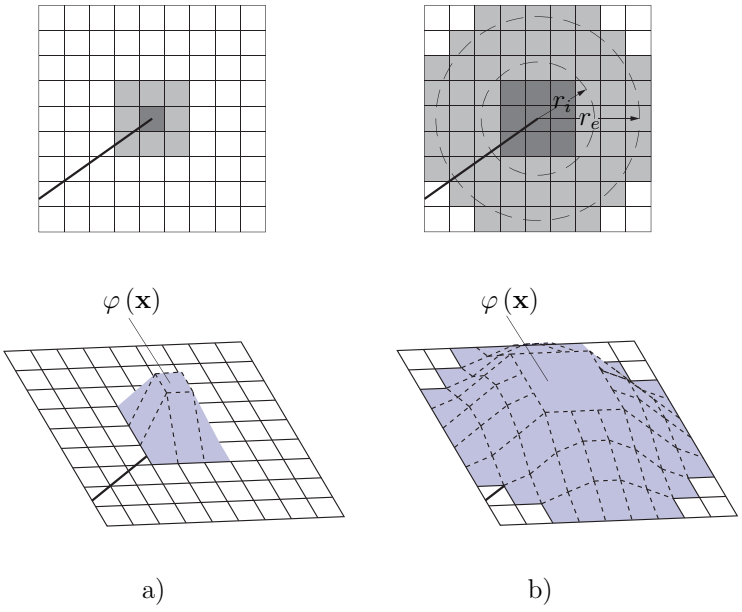

Fig. 5. Weight functions for a) topological and b) geometrical enrichment.

$$\varphi(\mathbf{x}) = \sum_{T \in \mathcal{N}^t} N_T(\mathbf{x})\, \varphi_T \tag{14}$$

where $\mathcal{N}^t$ is the set of tip enriched nodes and includes all nodes that belong to an element with at least one node inside the enrichment radius.

In Figure 5, an illustration of the definition of the weights for both of the cases mentioned above is given. For the second case, a linear ramp function is used.

Both of the above definitions refer to the weights used for tip enrichment functions. The weights for the jump enrichment functions are defined as:

$$\bar{\varphi}(\mathbf{x}) = 1 - \varphi(\mathbf{x}) \tag{15}$$

From the above it is clear that the distance r_i can be used to determine the length of the blending area (number of layers of blending elements). Moreover, in blending elements that contain the crack both jump and tip enrichment is used which as mentioned above is necessary when geometrical enrichment is used. By combining the above it can be concluded that a value close to the mesh parameter h should be chosen for parameter r_i. By adopting a sufficiently small value, it can be ensured that even for large values of the enrichment radius r_e all of the tip enriched elements that contain the crack, except from a small number of elements around the crack front, will also be jump enriched. It should be noted that if the enrichment radius r_e is given a smaller value than the value defined for r_i then the first definition for the weight functions is employed.

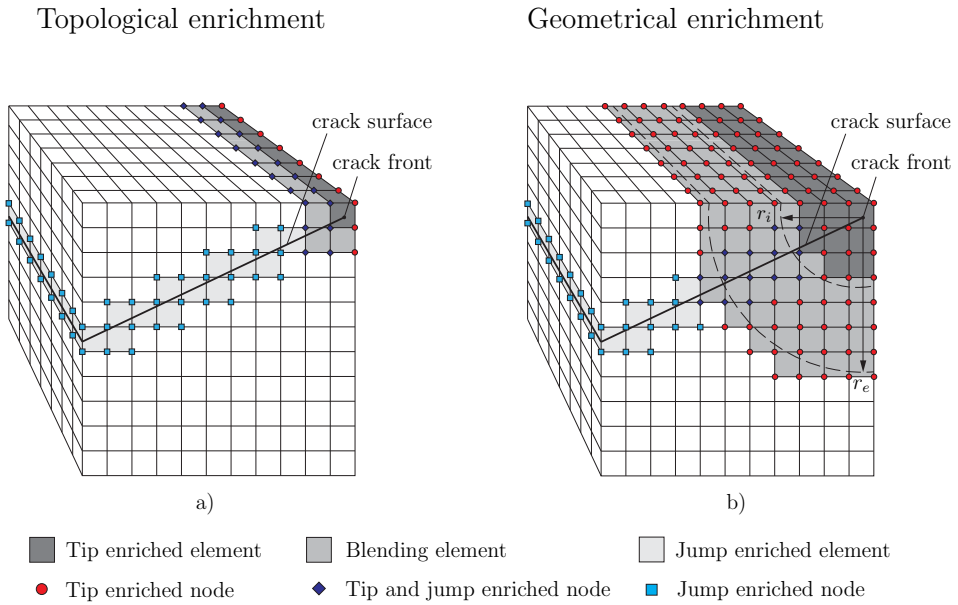

Fig. 6. Enrichment strategies used for tip and jump enrichment.

3.6 Enrichment function shifting

In Reference [23] two types of shifting are considered; the first consists in shifting the product of the weights and the enrichment functions, while the second consists in shifting only the enrichment functions and then weighting the shifted enrichment functions. It is demonstrated that only in the latter case the resulting approximation is different, and provides accuracy that is improved with respect to the standard XFEM approximation for both of the weight function definitions presented in the previous subsection. As a result, the second type of shifting will be used throughout this work. More details regarding the different types of shifting considered can be found in Reference [23].

Shifting of the tip enrichment functions is realized by obtaining the nodal values of the enrichment functions (multiplied by the front element shape functions), interpolating them using the finite element shape functions and subtracting them from the enrichment functions. Weighting, is realized by multiplying the shifted enrichment functions by the weight function:

$$\mathbf{u_t}(\mathbf{x}) = \underbrace{\varphi(\mathbf{x})}_{\text{weight function}} \left(\underbrace{\sum_{K \in \mathcal{N}^s} N_K^g(\mathbf{x}) \sum_i \sum_j F_{ij}(\mathbf{x})}_{\text{enrichment function}} - \right. \tag{16}$$

$$\left. - \underbrace{\sum_{T \in \mathcal{N}^t} N_T(\mathbf{x}) \sum_{K \in \mathcal{N}^s} N_K^g(\mathbf{x}_T) \sum_i \sum_j F_{ij}(\mathbf{x}_T)}_{\text{FE interpolant of the nodal values}} \right) \mathbf{c}_{Kij}$$

For jump enriched elements, simple nodal shifting is used:

$$\mathbf{u_j}(\mathbf{x}) = \bar{\varphi}(\mathbf{x}) \sum_{J \in \mathcal{N}^j} N_J(\mathbf{x}) (H(\mathbf{x}) - H_J) \mathbf{b}_J \tag{17}$$

where $\mathcal{N}^j$ is the set of jump enriched nodes and includes all nodes whose support is divided in two by the crack and in addition belong to elements where the weight function $\bar{\varphi}(\mathbf{x})$ assumes values greater than zero (Figure 6).

3.7 Displacement approximation

With all the above considerations in place, the displacement approximation for the proposed method is:

$$\begin{aligned} \mathbf{u}(\mathbf{x}) = & \sum_{I \in \mathcal{N}} N_I(\mathbf{x}) \mathbf{u}_I + \bar{\varphi}(\mathbf{x}) \sum_{J \in \mathcal{N}^j} N_J(\mathbf{x}) (H(\mathbf{x}) - H_J) \mathbf{b}_J + \\ & + \varphi(\mathbf{x}) \left(\sum_{K \in \mathcal{N}^s} N_K^g(\mathbf{x}) \sum_i \sum_j F_{ij}(\mathbf{x}) - \right. \\ & \left. - \sum_{T \in \mathcal{N}^t} N_T(\mathbf{x}) \sum_{K \in \mathcal{N}^s} N_K^g(\mathbf{x}_T) \sum_i \sum_j F_{ij}(\mathbf{x}_T) \right) \mathbf{c}_{Kij} \end{aligned} \tag{18}$$

where (see Figure 6):

$\mathcal{N}$ is the set of all nodes in the FE mesh.

$\mathcal{N}^j$ is the set of jump enriched nodes. This nodal set includes all nodes whose support is split in two by the crack and in addition belong to elements where the weight function $\bar{\varphi}(\mathbf{x})$ assumes values greater than zero.

$\mathcal{N}^t$ is the set of tip enriched nodes. This nodal set includes all nodes that belong to an element with at least one node inside the enrichment radius.
$\mathcal{N}^s$ is the set of nodes in the superimposed mesh defined in Subsection 3.2.

The displacement approximation of the method is quite simple and does not involve the introduction of special points along element boundaries as in [17]. As a result the extension of the method to higher order finite elements would be straightforward.

4 Element partitioning

Element partitioning and special coordinate transformations are employed in order to minimize numerical integration errors for the enriched part of the approximation. In the present work, an element partitioning algorithm similar to the one described in Loehnert et al. [24] is introduced which also accounts for the intersections of the standard with the superimposed mesh (Figure 7).

The algorithm is formulated in order to meet two main requirements. The first requirement is that it should allow each finite element to be intersected by several front elements, which is a situation that, depending on the enrichment radius and crack front geometry, could occur in practical applications. The second requirement demands that elements are divided into sub-elements according to their position relative to the zero isosurfaces defined by the level set functions as also performed in [24]. The algorithm is divided in two parts, each of which fulfills one of the aforementioned requirements:

(1) **Division into front elements.**

For each element, the number of intersecting front elements is determined using the minimum and maximum values of the front parameter. For each intersecting front element a discrete element part is created which comprising $f_e + 2$ faces, where f_e is the number of element faces. The additional faces are introduced to account for front element boundaries. Subsequently, element faces and edges are looped over and the intersections of each element edge with front element boundaries are found and assigned to the corresponding part and face. During this procedure nodal points are also assigned to element parts and faces according to their front parameter value. At the end of this phase, some faces may comprise the exact same nodes while others may not be assigned any nodes. In that case, before proceeding to the next phase, duplicate or empty faces are deleted. In addition, the nodes corresponding to each face are sorted using the method presented in [24]. This step of the algorithm is illustrated in Figure 8 b).

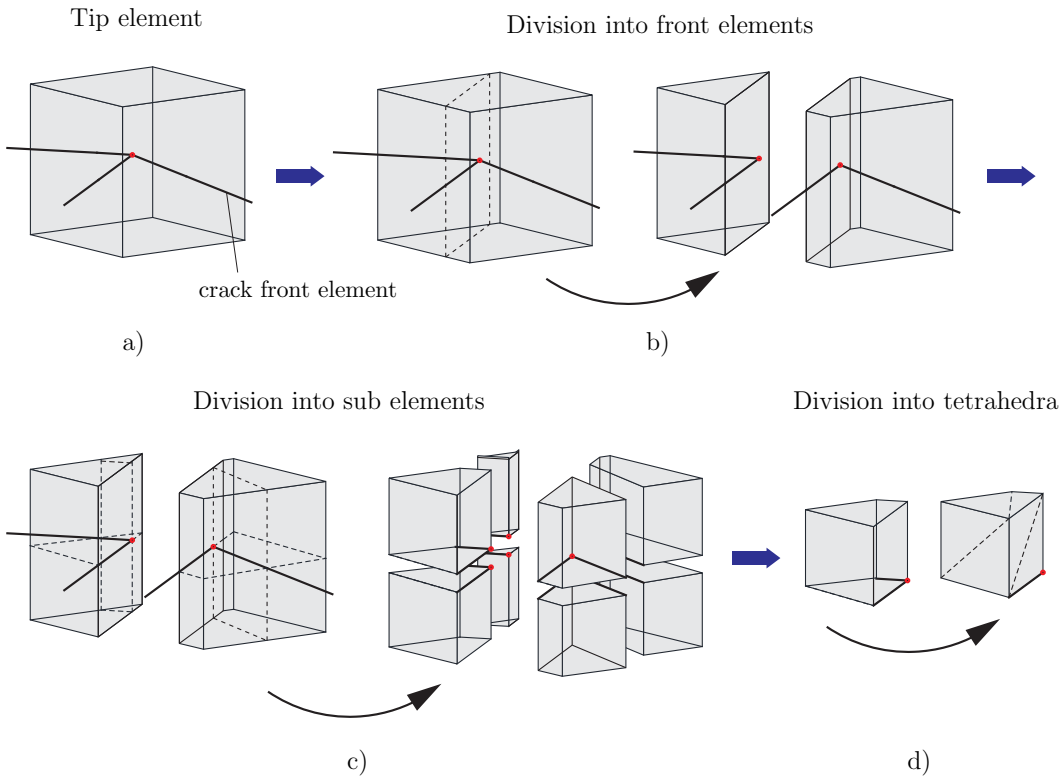

Fig. 7. Procedure used for element partitioning. a) Front element containing the crack front. b) The element is partitioned according to the front elements that intersect it. c) Each element part is further sub-divided by the zero isosurfaces of the level set functions. d) Each sub element is sub-divided into sub-tetrahedra.

(2) **Division into sub elements.**

Each part of the element defined in the previous step, is divided into sub-elements as shown in Figure 8 c) using the algorithm of Loehnert et al. [24]. Finally, each sub element is divided into tetrahedra (Figure 8 d)) using the following procedure:

- If the sub-element comprises exactly four faces, each of which consists of exactly three nodes, then the sub element is already a tetrahedron and no subdivision is necessary.
- In every other case, each face is divided into triangles according to the pattern illustrated in Figure 8, for triangular faces no subdivision is required. Tetrahedra are formed using three nodes from the previously defined triangles and the arithmetic mean of the nodal coordinates of the sub-element.

The motivation behind the use of the pattern described above is that in general the accuracy provided by Gauss integration depends on the number of points used in each tetrahedron and not on the number of tetrahedrons used to subdivide a given volume. As a result, subdividing each sub-element into the

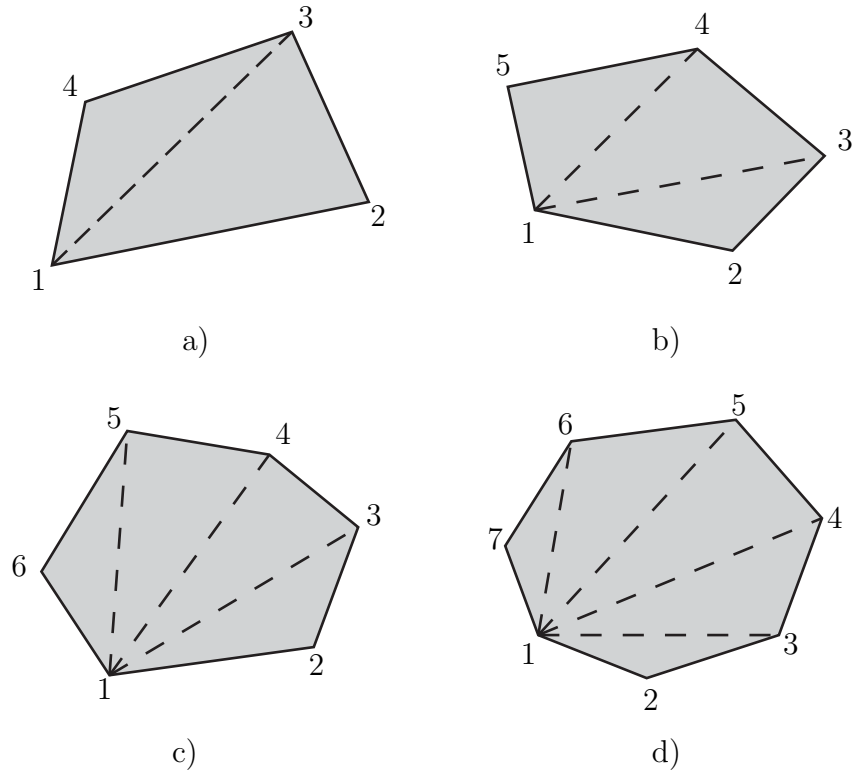

Fig. 8. Pattern used to subdivide sub-element faces into triangles.

least possible number of tetrahedrons and using a larger number of points for each tetrahedron should be much more efficient than subdividing each sub-element into a larger number of tetrahedra and using a smaller number of points in each tetrahedron. The number of tetrahedra created for each sub-element face by the proposed method is reduced by two tetrahedra compared to the method introduced in [24] which, considering the fact that according to our experience most faces consist of three to five nodes, results in a substantial reduction in the total number of tetrahedra created.

Similar approaches for partitioning elements are also used in several 2D implementations (e.g. [55,27]).

It should be noted that the proposed algorithm has been implemented both for hexahedral and tetrahedral elements.

The total computational cost associated with numerical integration is quite large and probably constitutes one drawback of the proposed approach. The primary reasons for the increased computational cost are summarized as follows:

- The use of geometrical enrichment requires the use of more accurate, and expensive, integration schemes for all the elements lying inside the area of enrichment. This drawback is associated with geometrical enrichment

in general.
- The additional element subdivisions required for the proposed method further increase the computational cost. This is especially true for elements containing the crack front, where quite a large number of Gauss points is necessary for each sub-tetrahedron. This additional cost is only associated with the proposed method.

In order to improve the above situation, special numerical integration techniques could be employed, which decrease the number of Gauss points required for each sub-tetrahedron, for instance a 3D extension of the method proposed by Chevaungeon et al. [27]. As an alternative, generalized Gaussian quadrature rules [32] could be used to reduce the total number of points required for each element.

5 SIF evaluation

In Reference [17] we employed an SIF evaluation method similar to the one of References [4,5] was employed. That procedure involved the use of a parallelepiped mesh around each point of interest. One problem with that approach however, is that in order to properly account for the tractions applied at the crack surfaces, a very large number of elements ($8 \times 8 \times 8$) and a large number of Gauss points for each element ($6 \times 6 \times 6$) must be used for the additional mesh.

Since this procedure is computationally impractical and was only used to provide a fair estimate of the accuracy of the proposed method, compared to the literature, in the following subsections an alternative approach is described, which simplifies SIF evaluation even for the case when surface tractions are applied along the crack surfaces.

5.1 Interaction integral

Stress intensity factors are evaluated here using the interaction integral. For the case where surface tractions are applied on the crack faces, an additional term is added as in Walters et al. [56]:

$$I = -\int_V q_{i,j}\left(\sigma_{kl}\epsilon^{\text{aux}}_{kl}\delta_{ij} - \sigma^{\text{aux}}_{kj}u_{k,i} - \sigma_{kj}u^{\text{aux}}_{k,i}\right)dV - \int_V q_i\left(\sigma^{\text{aux}}_{kl,i}\epsilon_{kl}\delta_{ij} - \sigma_{kl}u^{\text{aux}}_{k,li} - \sigma^{\text{aux}}_{kl,l}u_{k,i}\right)dV - \int_{\Gamma^t_{c+}\cup\Gamma^t_{c-}}\left(t_j u^{\text{aux}}_{j,i}\right)q_i d\Gamma \quad (19)$$

where ϵ^{aux}, σ^{aux} and u^{aux} are the auxiliary stress, strain and displacement fields respectively which are defined as in Moës et al. [5], q_i are the components of the virtual velocity field and t_j are the applied surface tractions. The additional term is integrated over the crack faces Γ^t_{c+} and Γ^t_{c-}.

Tensors in the above equation refer to a basis defined by the level set gradients as in Moës et al. [5,6]. The base vectors used are modified such that they form an orthogonal basis as in [47,48].

The interaction integral of Equation 19 is evaluated in an extraction domain which will be defined in the following subsection. If the integrand of Equation 19 is assumed to vary very slowly along the crack front, then the point-wise value of the interaction integral, which is necessary in order to obtain the SIF values, can be obtained as:

$$I_p = \frac{I}{\int_{L_c} q_1(s)\, ds} \tag{20}$$

where s is a variable that runs along the length of the crack front and L_c is the length of the extraction domain along the crack front.

5.2 Interaction integral domain and virtual velocity field

The domain in which the integral of Equation 19 is evaluated is essentially determined by the definition of the virtual velocity field q_i. In contrast to [17] and to several other XFEM implementations [4,5,48], we will use a definition similar to the one used in 2D implementations ([3,47]). More precisely, given the set of points $\mathbf{x_p}$ where the SIFs are to be computed and the distances r_1, r_2, r_3 used for SIF evaluation, the level set gradients are computed at each point and the distance from point $\mathbf{x_p}$ along the direction of vector $\mathbf{e_3}$ for a given point $\mathbf{x}$ is defined as:

$$x_{3p} = (\mathbf{x} - \mathbf{x_p}) \cdot \mathbf{e_{3p}} \tag{21}$$

where $\mathbf{e_{3p}}$ denotes vector $\mathbf{e_3}$ evaluated at point $\mathbf{x_p}$.

Subsequently the nodal values of the first component of the virtual velocity field can be computed as:

$$q_1 = \begin{cases} 1 \text{ if } \phi \leq r_1 \text{ and } \psi \leq r_2 \text{ and } x_{3p} \leq r_3 \\ 0 \text{ if } \phi > r_1 \text{ or } \psi > r_2 \text{ or } x_{3p} > r_3 \end{cases} \tag{22}$$

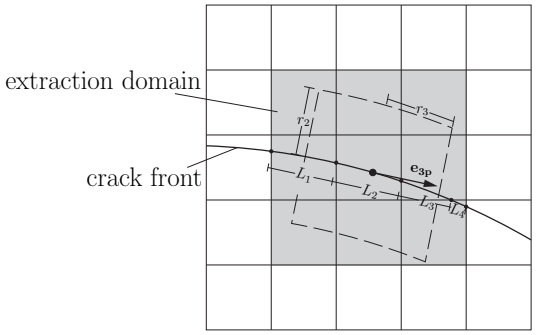

Fig. 9. Computation of the projected lengths of the individual line segments forming segment L_c.

the other two components q_2 and q_3 assume a value of zero. In the interior of elements, the virtual velocity field is interpolated using the FE shape functions.

By using the above definition, the extraction domain used for the interaction integral for a point $\mathbf{x_p}$, corresponds to the set of elements having at least one node inside the volume defined by Equation 22.

The element-wise definition of the extraction domain also implies that the length of segment L_c along the crack front is no longer fixed and the integral in the denominator of Equation 20 has to be computed for each evaluation point. This can be achieved by considering the crack front as a series of line segments and by computing the integral along each of those segments. The endpoints of those segments are the points where the crack front intersects enriched elements and should have already been computed during the element partitioning algorithm of Section 4.

It has been observed that in order to obtain the correct SIFs, during the computation of segment L_c instead of the actual length of the line segment corresponding to each element, the projection of this length in the direction of vector $\mathbf{e_{3p}}$ has to be used. This is because during SIF evaluation, the variation of the level set gradients is ignored and as a result vector $\mathbf{e_3}$ is constant and coincides with vector $\mathbf{e_{3p}}$ for the whole extraction domain corresponding to point p. The computation of the projected line segment lengths is illustrated in Figure 9.

The use of the above definition of the virtual velocity field and interaction integral domain can be justified by a comparison with some alternative definitions. In Figure 10 a 2D visualization of three different approaches is given in order to facilitate the comparison.

In the first approach (Figure 10 a)), used in References [4,5,17], an orthogonal mesh is introduced for the evaluation of the interaction integral and the virtual velocity field is essentially defined on that mesh. By using this definition, the virtual velocity field can be integrated exactly, since the Gauss points used are

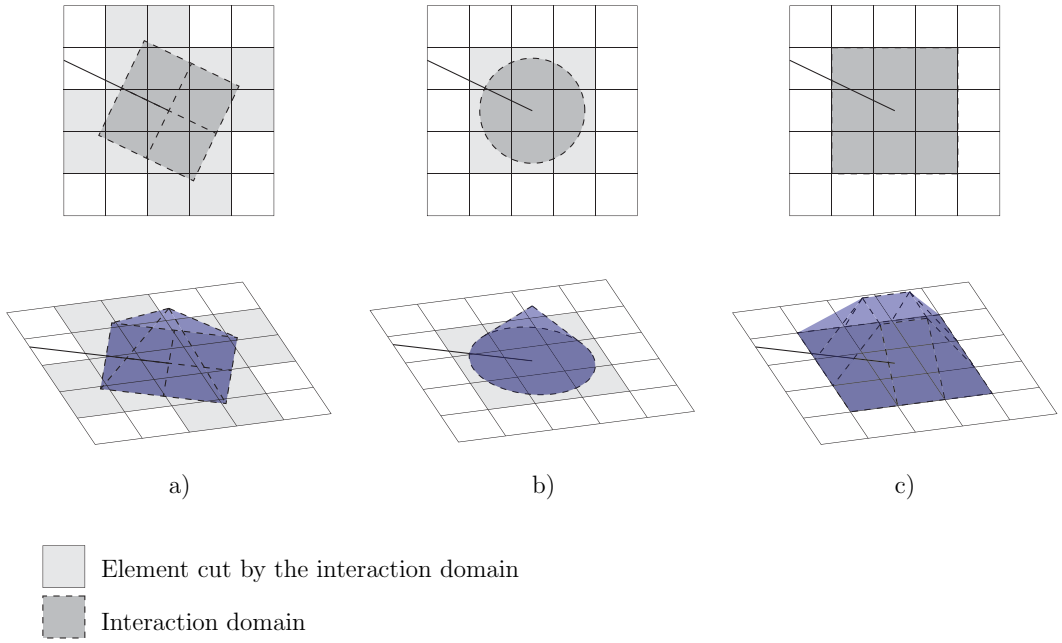

Fig. 10. Three different approaches for the definition of the interaction domain and the virtual velocity field. a) Definition given in References [4,5,17]. b) Definition given in Reference [48]. c) Proposed approach, also used in 2D implementations ([3,47]).

the ones corresponding to the additional mesh. The accuracy in the integration of the stress, strain, and displacement gradient fields however is reduced since those fields are defined on the FE mesh and the Gauss points used do not account for their variation properly. One remedy for this would be the use of a large number of Gauss points which would also increase the computational cost significantly.

According to the second approach (Figure 10 b)), which is adopted in Reference [48], the virtual velocity field and interaction integral domain are defined independently of the FE mesh and numerical integration is carried out at the element level. In this approach the stress, strain and displacement gradient fields are integrated properly since the numerical integration schemes used for the integration of the element matrices can be employed. Nevertheless, the virtual velocity fields cannot be integrated accurately since the numerical integration schemes used do not account for the boundaries of the interaction integral domain.

Finally, the proposed definition (Figure 10 c)), which has been successfully employed in 2D implementations ([3,47]), uses FE shape functions for the definition of the virtual velocity field. In addition, the interaction integral domain boundaries coincide with element boundaries. As a result, both the virtual velocity and the stress, strain and displacement gradient fields can be appropriately integrated by the improved integration schemes used for the

integration of the element stiffness matrices.

5.3 Integration of the surface tractions applied on the crack faces

By using the element partitioning algorithm of Section 4 the points where the crack intersects elements as well as the corresponding surfaces should already be available and divided into triangles. As a result, the only necessary action to proceed with the evaluation of the third integral of Equation 19 is to displace those surfaces by a negative and a positive increment along the direction of the level set gradient that is normal to the crack surface in order to obtain the upper and lower crack faces Γ_{c+}^{t} and Γ_{c-}^{t}.

In order to improve the accuracy of the computed SIFs and since, as also noted in Walters et al. [56], the contribution of the surface tractions to the SIFs is significant, a special procedure is introduced for the integration of surface tractions at the crack faces. This procedure involves a coordinate transformation similar to the one performed in [56]. Nevertheless, since in the present work numerical integration has to be carried out for triangles whose sides do not necessarily coincide with the crack front or with the iso-lines of the level set functions, the transformation has to be modified accordingly.

Prior to performing the transformation, a coordinate system has to be defined for each triangle which consists of the two polar coordinates r and θ and a third coordinate which is approximately parallel to the direction of the crack front. This third coordinate for a given point $\mathbf{x}$ lying on the surface of the triangle is defined by evaluating vector $\mathbf{e_3}$ at the midpoint of the triangle ($\mathbf{x_t}$) and applying the formula:

$$z_c = (\mathbf{x} - \mathbf{x_t}) \cdot \mathbf{e_{3t}} \tag{23}$$

where $\mathbf{e_{3t}}$ is vector $\mathbf{e_3}$ evaluated at the midpoint of the triangle.

The definition of the coordinate system is illustrated in Figure 11 for a node of an arbitrary triangle.

Since the triangles lie on the crack surface, angle θ assumes a value of zero and radius r is equal to the absolute value of the second level set ψ.

Once the coordinate system has been defined, the transformation takes the form:

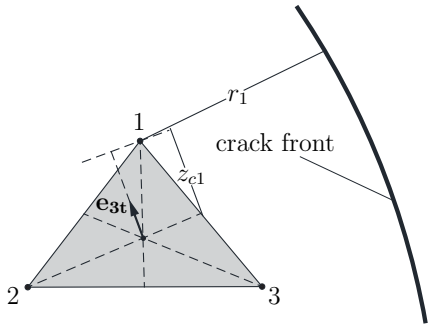

Fig. 11. Coordinates r and z_c for a node 1 of the arbitrary triangle 1-2-3 lying on the crack surface.

$$\left.\begin{array}{l} \bar{r} = \sqrt{r} \\ \bar{z}_c = z_c \end{array}\right\} \tag{24}$$

The inverse transformation writes:

$$\left.\begin{array}{l} r = \bar{r}^2 \\ z_c = \bar{z}_c \end{array}\right\} \tag{25}$$

In order to produce a scheme that achieves exact integration the area of the triangles and provides increased accuracy for the last integral of Equation 19 the following procedure is followed:

- The coordinates r and z_c of the triangle nodes are computed and transformed to the $\bar{r}, \bar{z}_c$ system using the transformation of Equation 24 (Figure 12 b)).
- The sides of the triangle in the transformed system become curves which can be represented exactly by second order polynomials. As a result the transformed triangles can be represented exactly by quadratic triangles.
- For the definition of the quadratic triangles corresponding to the transformed triangles, additional points that lie on the sides of the triangles are required (Figure 12 c)). For a given side of a triangle with nodal coordinates $\bar{r}_a, \bar{z}_{ca}$ and $\bar{r}_b, \bar{z}_{cb}$, the coordinates of those points are computed using the following expression:

$$
\begin{aligned}
&\text{if } (\bar{r}_a \neq \bar{r}_b) \\
&\left.\begin{aligned}
&\bar{r}_m = \tfrac{\bar{r}_a + \bar{r}_b}{2} \\
&\bar{z}_{cm} = \bar{z}_{ca} + \frac{(\bar{r}_m^2 - \bar{r}_a^2)\,(\bar{z}_{cb} - \bar{z}_{ca})}{\bar{r}_b^2 - \bar{r}_a^2}
\end{aligned}\right\} \\
&\text{else} \\
&\left.\begin{aligned}
&\bar{r}_m = \bar{r}_a = \bar{r}_b \\
&\bar{z}_{cm} = \frac{\bar{z}_{ca} + \bar{z}_{cb}}{2}
\end{aligned}\right\}
\end{aligned}
\tag{26}
$$

where $\bar{r}_m, \bar{z}_{cm}$ are the coordinates of the additional points. In order to derive the above expressions, the equation of the line segment a-b is transformed to the $\bar{r}, \bar{z}_c$ system, the coordinate $\bar{r}$ is given the value $\bar{r}_m$ and the equation is solved for variable $\bar{z}_c$. It need be noted that, for the case where $\bar{r}_a = \bar{r}_b$ the equation cannot be solved and the alternative values have to be given to the coordinates $\bar{r}_m$ and $\bar{z}_{cm}$.

- The coordinates of the Gauss points for the quadratic triangles in the $\bar{r}, \bar{z}_c$ system are computed. The Gauss points are first obtained in the local triangular coordinates of each triangle (as defined for instance in [57]) and then transformed in the 'global' system $\bar{r}, \bar{z}_c$ using the quadratic triangle shape functions (Figure 12 c)).
- The coordinates of the Gauss points are transformed back into the r, z_c system using the inverse transformation of Equation 25 (Figure 12 d)).
- If needed, coordinates r and z_c of the Gauss points can be transformed in the local coordinate system of the triangles.

For a straight crack front and a planar crack the above procedure should integrate the crack surface and the singular functions exactly. For curved crack fronts and crack surfaces some errors might be introduced, which should however decrease as the meshes become finer.

The whole procedure shares some similarities with the integration scheme proposed in Chevaugeon et al. [27].

6 Numerical examples

The energy and L_2 error norms used throughout this subsection are defined as follows, where it is noted that vectors and tensors are written in matrix form:

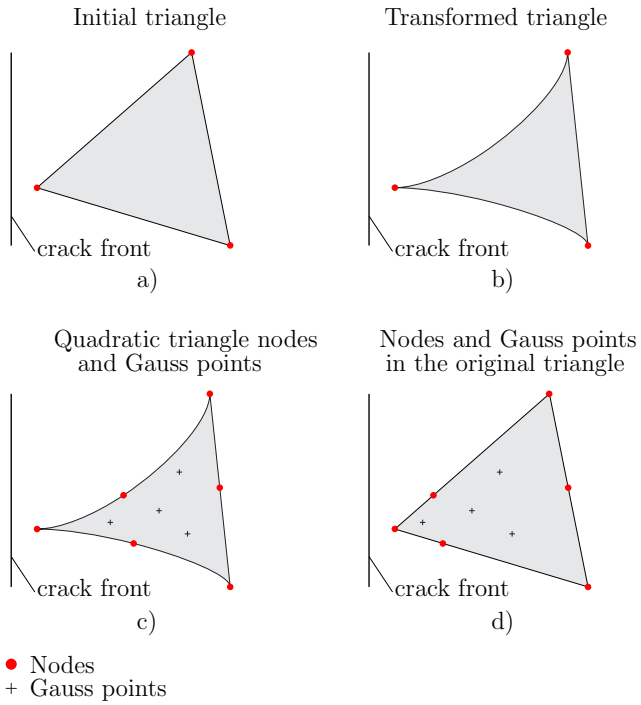

Fig. 12. Integration scheme for an arbitrary triangle lying on the crack surface.

$$E = \left(\frac{\int_\Omega (\boldsymbol{\epsilon} - \boldsymbol{\epsilon}^h)^T \boldsymbol{D} (\boldsymbol{\epsilon} - \boldsymbol{\epsilon}^h) \, d\Omega}{\int_\Omega \boldsymbol{\epsilon}^T \boldsymbol{D} \boldsymbol{\epsilon} \, d\Omega} \right)^{1/2} \tag{27a}$$

$$L_2 = \left(\frac{\int_\Omega (\boldsymbol{u} - \boldsymbol{u}^h)^T (\boldsymbol{u} - \boldsymbol{u}^h) \, d\Omega}{\int_\Omega \boldsymbol{u}^T \boldsymbol{u} \, d\Omega} \right)^{1/2} \tag{27b}$$

where $\boldsymbol{\epsilon}$ and $\boldsymbol{u}$ are the strains and displacements obtained from the analytical solution and $\boldsymbol{\epsilon}^h$ and $\boldsymbol{u}^h$ are the corresponding numerically obtained values.

For the implementation of the proposed method, a C++ code was created utilizing the Gmm++ library [58] for linear algebra operations. For the solution of the systems of equations, the conjugate gradient (CG) solver of the Gmm++ package was employed in combination to a diagonal preconditioner. The convergence tolerance for the solver was set to 10^{-8}. The unstructured meshes used were generated using the gmsh mesher [59].

The acronyms used for the different methods tested are described in Table 1. It should be noted that results obtained using the method introduced in our previous work [17] will also be given, in some of the examples, for reference.

Acronym	Description
XFEM	Standard XFEM (with shifted enrichment functions)
GE-XFEM	Global Enrichment XFEM
CGE-XFEM	Continuous Global Enrichment XFEM
CGE-XFEM-2 terms	Continuous Global Enrichment XFEM with 2 terms of the Williams expansion
CGE-XFEM-4 terms	Continuous Global Enrichment XFEM with 4 terms of the Williams expansion

Table 1
List of acronyms used for the 3D convergence study.

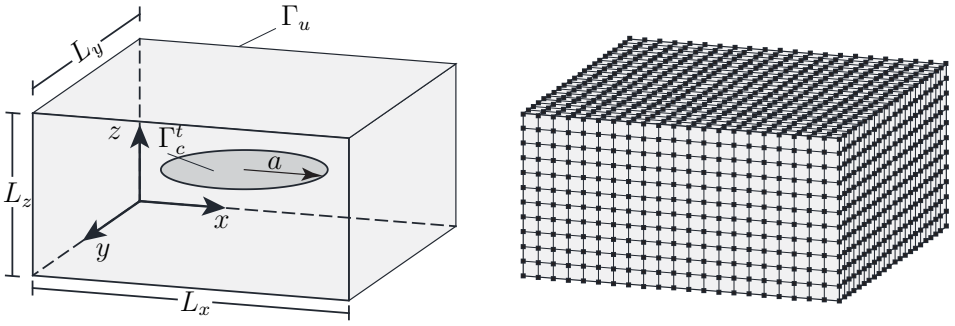

■ node where boundary conditions are applied

Fig. 13. Penny crack problem geometry and discretization. The boundary conditions provided by the analytical solution are imposed along the boundaries of the domain. Uniform normal and shear loads are applied to the crack surfaces. The dimensions of the problem are $L_x = L_y = 2L_z = 0.4$ units and $a = 0.1$ unit. For CGE-XFEM errors keep decreasing as the enrichment radius is increased,

6.1 3D convergence study

The first benchmark problem studied in this section is identical to the one introduced in [17]. More specifically, the problem of a penny crack in an infinite solid subjected to uniform normal and shear loading is considered. Only a parallelepiped part of the domain around the crack is considered and the displacement fields obtained by the analytical solution [60] are imposed as constraints at the boundaries of the domain. Additionally, uniform normal and shear loads are applied at the crack faces. The problem is illustrated in Figure 13.

The dimensions of the domain were set to $L_x = L_y = 2L_z = 0.4$ units and the radius of the crack is taken as $a = 0.1$ unit. A uniform normal and a uniform shear load of magnitude 1 are applied at the crack faces (mixed mode loading). The material parameters used are $E = 100$ units and $\nu = 0.3$.

A series of hexahedral meshes was used consisting of $n_x \times n_y \times n_z$ elements where $n_x = n_y = 2n_z = n$ and $n \in \{21, 41, 61, 81, 101\}$. The crack front was

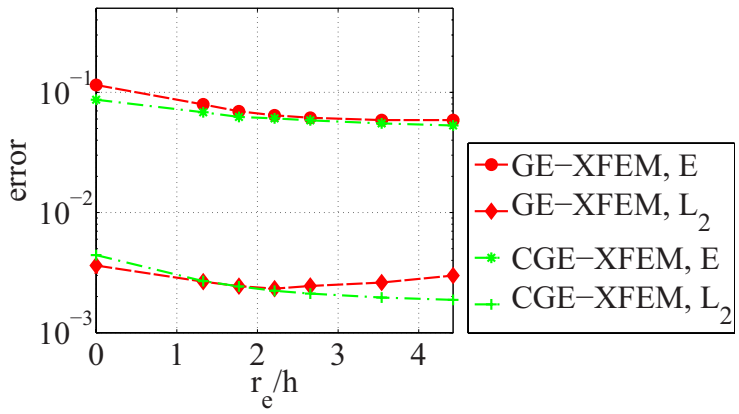

Fig. 14. Penny crack problem. Influence of the enrichment radius (r_e) in the energy (E) and L_2 norms for two variations of the proposed method described in Table 1. The radius of the crack is $a = 0.1$ units and the size of the domain is $L_x = L_y = 2L_z = 0.4$ units. Results refer to a mesh of $31 \times 61 \times 61$ elements. h denotes the mesh parameter. The proposed method (CGE-XFEM) provides increased accuracy and similar convergence rates to standard XFEM.

discretized using 32 front elements for the $11 \times 21 \times 21$ and $21 \times 41 \times 41$ meshes and 64 front elements for the rest of the meshes.

6.1.1 L_2 and energy norms

In Figure 14 the influence of the enrichment radius (r_e) on the energy and L_2 norms is examined. It can be seen that the continuous version of the proposed method solves the problems encountered by the method of Reference [17] since the errors keep decreasing as the enrichment radius is increased.

Energy and L_2 norms are plotted in Figures 15 and 16 for topological ($r_e = 0.00$ units) and geometrical ($r_e = 0.02$ and $r_e = 0.04$ units) enrichment for all methods considered herein, while the corresponding convergence rates are given in Table 2. Again it can be noticed that CGE-XFEM solves the problems encountered in the discontinuous version of the method and provides improved accuracy and optimal convergence rates for both the energy and the L_2 norm.

In Figure 17 the effect of the addition of higher order enrichment functions on the accuracy of the method is studied. The addition of the higher order terms provides a reduction of up to 17% in the L_2 norm and 15% in the energy norm. It should be noted however, that for the finer meshes the reduction of the errors, especially in the L_2 norm, is smaller when only two terms of the Williams expansion are employed. Moreover, a larger number of terms is required (4 terms in total) in order to achieve a significant error reduction. This is expected since for finer meshes the standard part of the approximation is able itself to reproduce the higher order terms (smoother than the first few terms).

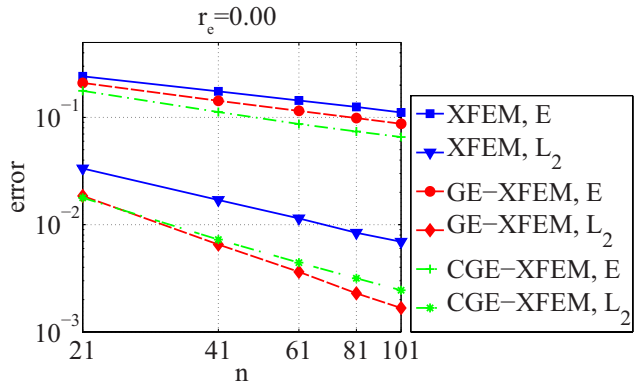

Fig. 15. Penny crack problem. L_2 and energy (E) norms versus the number of elements along the largest sides (n) for topological enrichment ($r_e = 0.00$ units) for mixed mode loading. The radius of the crack is $a = 0.1$ units and the size of the domain is $L_x = L_y = 2L_z = 0.4$ units. A description of the different methods mentioned in the figure is given in Table 1, while the corresponding convergence rates are given in Table 2.

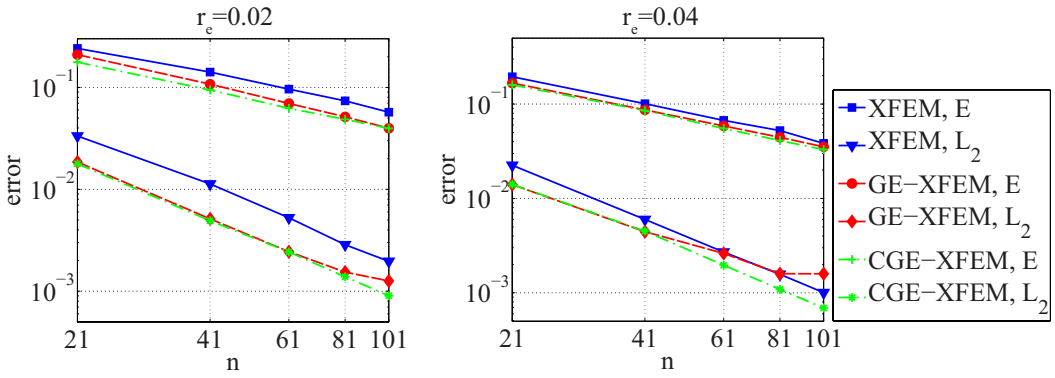

Fig. 16. Penny crack problem. L_2 and energy (E) norms versus the number of elements along the largest sides (n) for geometrical enrichment with enrichment radii $r_e = 0.02$ units and $r_e = 0.04$ units for mixed mode loading. The radius of the crack is $a = 0.1$ units and the size of the domain is $L_x = L_y = 2L_z = 0.4$ units. A description of the different methods mentioned in the figure is given in Table 1, while the corresponding convergence rates are given in Table 2. The proposed method (CGE-XFEM) provides improved accuracy both in the L_2 and the energy error norm.

6.1.2 Stress intensity factors

Stress intensity factors were computed for the proposed method and standard XFEM using the procedure described in Section 5. In Figure 18, errors in the SIFs are illustrated as functions of the angle θ for two different meshes ($21 \times 41 \times 41$ and $41 \times 81 \times 81$) for geometrical ($r_e = 0.04$) enrichment. Due to symmetry only the values for $0° \leq \theta \leq 90°$ are presented. The distances r_1, r_2, r_3 are assigned the values of $r_1 = 2h, r_2 = 2h, r_3 = 2h$. Results using higher order enrichment functions were not included in this comparison since

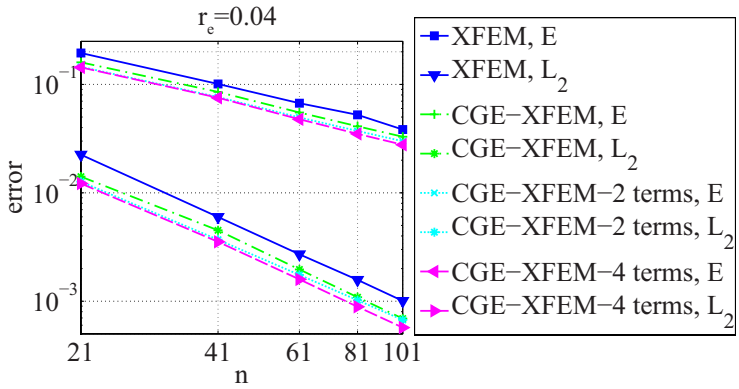

Fig. 17. Penny crack problem. L_2 and energy (E) norms versus the number of elements along the largest sides (n) for geometrical enrichment with enrichment radius $r_e = 0.04$ units for mixed mode loading. The radius of the crack is $a = 0.1$ units and the size of the domain is $L_x = L_y = 2L_z = 0.4$ units. A description of the different methods mentioned in the figure is given in Table 1, while the corresponding convergence rates are given in Table 2. The addition of higher order terms provides some additional improvement in the accuracy of the results.

	$r_e = 0.00$	$r_e = 0.02$	$r_e = 0.04$
XFEM E	0.492	0.911	1.015
XFEM L_2	1.009	1.824	1.976
GE-XFEM E	0.558	1.057	0.988
GE-XFEM L_2	1.535	1.753	1.448
CGE-XFEM E	**0.635**	**0.957**	**1.014**
CGE-XFEM L_2	**1.265**	**1.890**	**1.930**
CGE-XFEM-2 terms E	-	-	**1.013**
CGE-XFEM-2 terms L_2	-	-	**1.870**
CGE-XFEM-4 terms E	-	-	**1.055**
CGE-XFEM-4 terms L_2	-	-	**1.953**

Table 2
Penny crack problem. Convergence rates for the curves of Figures 15 and 16 for the energy (E) and L_2 norms for topological ($r_e = 0.00$) and geometrical ($r_e = 0.02$ units and $r_e = 0.04$ units) enrichment.

for this specific example they only slightly improve the computed SIFs.

The improved accuracy compared to our previous work [17] may be attributed to the use of a larger enrichment radius ($r_e = 0.04$ units compared to $r_e = 0.00$ units and $r_e = 0.02$ units in [17]) and the use of the improved SIF evaluation procedure. A comparison of the two methods, however, is not straightforward due to the different definitions of the interaction integral domain.

It can be noted that the accuracy of the SIFs provided by the proposed method is very close to the one achieved by standard XFEM, in fact in some areas the lines are almost indistinguishable. Nevertheless, the systems of equations produced by standard XFEM with geometrical enrichment, which is essential

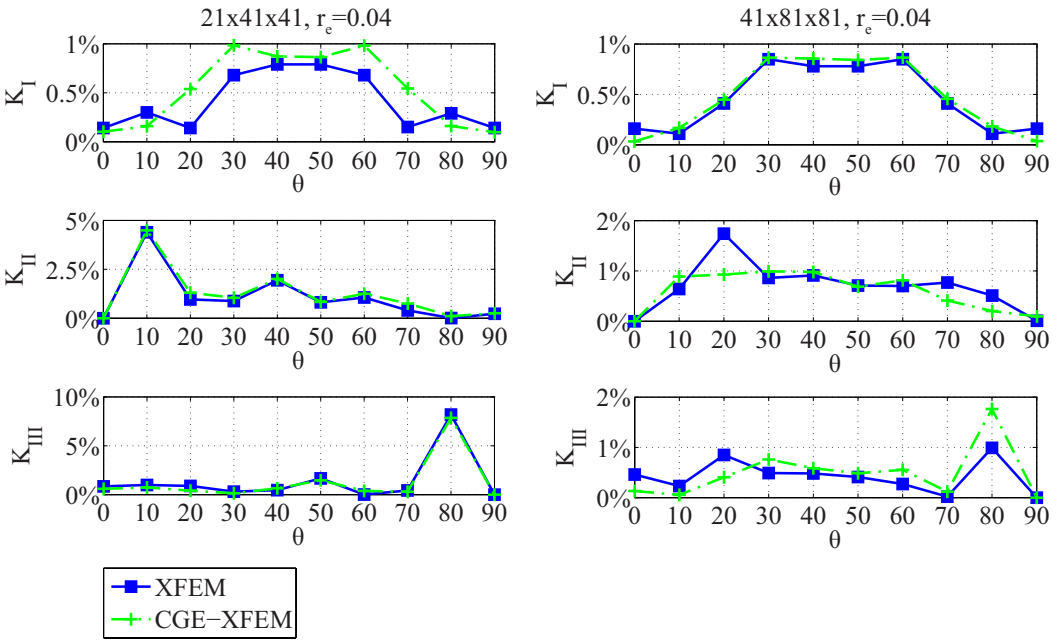

Fig. 18. Penny crack problem. Mode I, II and III stress intensity factors predicted by CGE-XFEM for geometrical ($r_e = 0.04$ units) enrichment for the $21 \times 41 \times 41$ and $41 \times 81 \times 81$ meshes. The radius of the crack is $a = 0.1$ units and the size of the domain is $L_x = L_y = 2L_z = 0.4$ units.

to obtain the increased accuracy and optimal convergence, are almost unsolvable. As a result, the proposed method provides a significant advantage as far as the extraction of accurate SIFs is concerned.

The convergence behavior has also been improved and, although convergence is slow and several fluctuations occur, errors tend to decrease with mesh refinement. The above behavior is displayed in Figure 19 where the average error for the Mode I, II and III SIFs is plotted against the number of elements along the largest sides (n) of the domain.

In Figure 19 an additional mesh was added consisting of $81 \times 161 \times 161$ elements, to verify that despite the fluctuations observed, the errors in the SIFs tend to decrease.

6.1.3 Conditioning

In order to assess the conditioning of the resulting system matrices, the number of iterations required by the solver to reach the predefined tolerance (10^{-8}) is reported. In Figure 20, a comparison is made between the number of iterations required by the solver for the three methods considered and for different enrichment radii. It is clear that the continuous version of the method further improves conditioning for the case of geometrical enrichment since the number of iterations required is practically independent of the enrichment radius used.

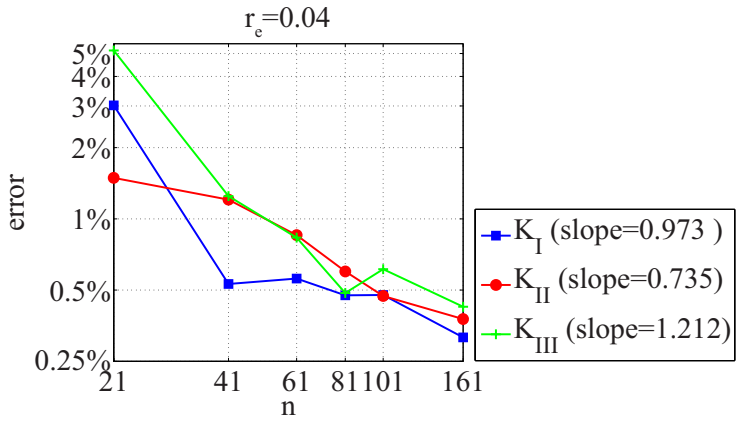

Fig. 19. Penny crack problem. Average error for the mode I, II and III stress intensity factors versus the number of elements along the largest sides (n) predicted by CGE-XFEM for geometrical ($r_e = 0.04$ units) enrichment. The radius of the crack is $a = 0.1$ units and the size of the domain is $L_x = L_y = 2L_z = 0.4$ units.

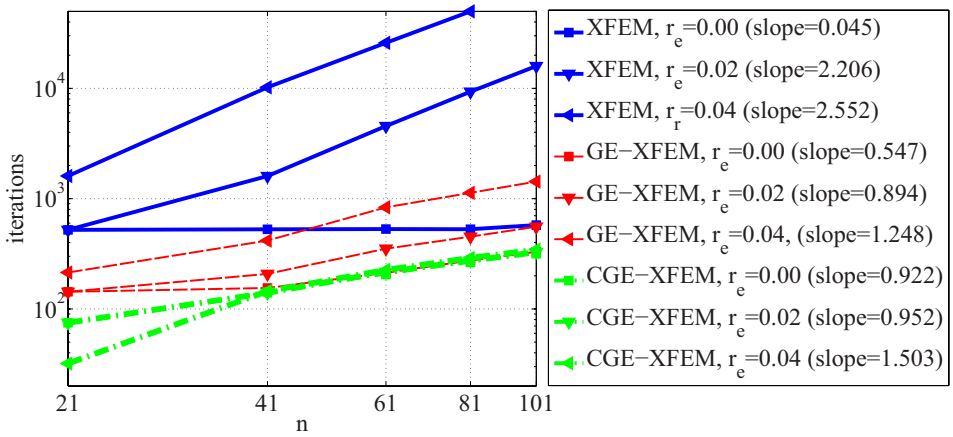

Fig. 20. Penny crack problem. Number of iterations required to solve the system of equations produced by XFEM, GE-XFEM and the proposed method versus the number of elements along the largest sides (n) for three different enrichment radii: $r_e = 0.00$ units (topological enrichment), $r_e = 0.02$ units and $r_e = 0.04$ units (geometrical enrichment). The tolerance of the CG solver was set to 10^{-8}. The radius of the crack is $a = 0.1$ units and the size of the domain is $L_x = L_y = 2L_z = 0.4$ units. The proposed method reduces the required number of iterations in every case.

In Figure 21, the number of iterations required by the proposed method when higher order enrichment functions are used is compared to two other methods for the geometrical enrichment case ($r_e = 0.04$ units). Although the behavior is oscillatory, the number of iterations when higher order terms are used is similar to the one required by the discontinuous version of the method (GE-XFEM).

In Figure 22 the error achieved by the solver after different iterations is calculated as in Menk and Bordas [16] for topological and geometrical enrichment and two different meshes. It is again confirmed that the behavior of the pro-

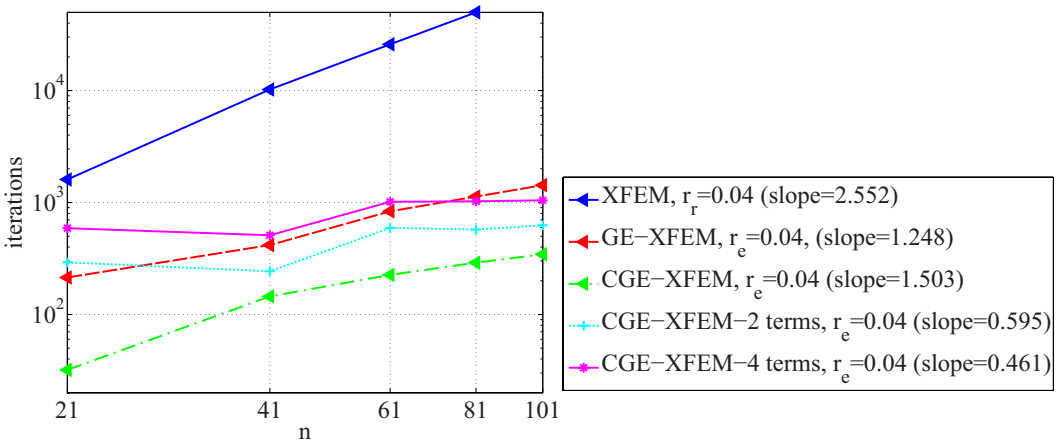

Fig. 21. Penny crack problem. Number of iterations required to solve the system of equations produced by XFEM, GE-XFEM and the proposed method with the addition of different number of higher order terms versus the number of elements along the largest sides (n) for an enrichment radius $r_e = 0.04$ units (geometrical enrichment). The tolerance of the CG solver was set to 10^{-8}. The radius of the crack is $a = 0.1$ units and the size of the domain is $L_x = L_y = 2L_z = 0.4$ units. The proposed method reduces the required number of iterations in every case.

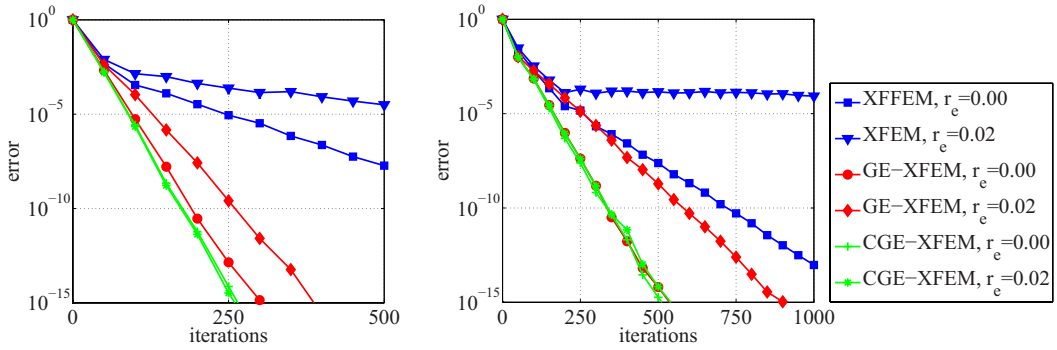

Fig. 22. Penny crack problem. Comparison of the performance of the PCG solver for XFEM, GE-XFEM and the proposed method. Results are shown for two different meshes consisting of $21 \times 41 \times 41$ and $41 \times 81 \times 81$ elements. Both topological ($r_e = 0.00$ units) and geometrical enrichment ($r_e = 0.02$ units) are considered. The behavior of CGE-XFEM is independent of the enrichment radius.

posed method is almost independent of the enrichment radius used.

6.2 Lens shaped crack

The last problem is that of a lens shaped crack in an infinite medium and has been used as a benchmark in other works as well [61,5]. In order to minimize boundary effects, a cube of side $L = 1$ unit is considered with a lens crack of radius $R = 0.2$ units and an angle $\alpha = \pi/4$. Young's modulus and Poisson's ratio are given values of $E = 68.9$ units and $\nu = 0.22$. A uniform unit stress

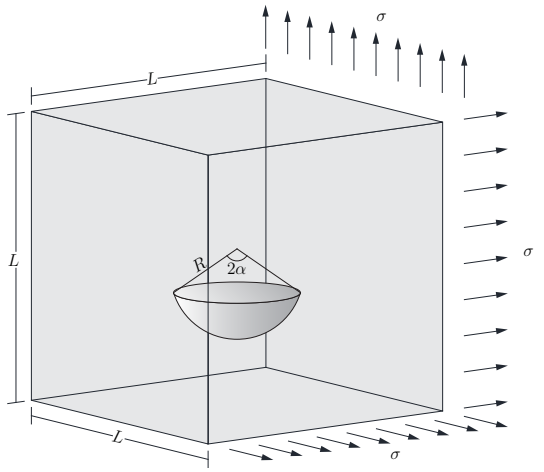

Fig. 23. Lens crack problem geometry and loading. The dimensions of the problem are $L = 1$ units, $R = 0.2$ units and $\alpha = \pi/4$. The uniform stress has a magnitude $\sigma = 1$ unit.

σ is applied in all three directions.

In our computations, an unstructured tetrahedral mesh is adopted with the mesh parameter h assuming a value $h = 0.25$ at the boundaries of the domain and a value of $h = 0.01$ $(R/20)$ in the vicinity of the crack. The number of standard degrees of freedom is approximately $150,000$. For the proposed method 64 front elements were used to discretize the crack front.

The material, geometry and mesh parameter values given above were all chosen to be as close as possible to the ones used in Moës et al. [5] so that the results obtained in that work can be used as a reference.

The distances used for SIF evaluation were given the smallest possible values $r_1 = h$, $r_2 = h$ and $r_3 = 2h$ in order to minimize errors caused by the fact that the crack curvature is ignored in the SIF evaluation procedure.

The analytical solution to this problem was obtained by Martynenko and Ulitko [62]. For the specific values of the parameters used, the SIFs assume the values ([61]):

$$K_I = 0.877\frac{2}{\pi}\sigma\sqrt{\pi a}, \qquad K_{II} = 0.235\frac{2}{\pi}\sigma\sqrt{\pi a} \tag{28}$$

where $a = r\cos(\alpha)$.

In Figure 24 the errors in the Mode I and II SIFs are given for standard XFEM and the proposed method for topological ($r_e = 0.00$ units) and geometrical ($r_e = 0.04$ units) enrichment. For the latter case, results are also given for enrichment functions involving one higher order term (two terms of the ex-

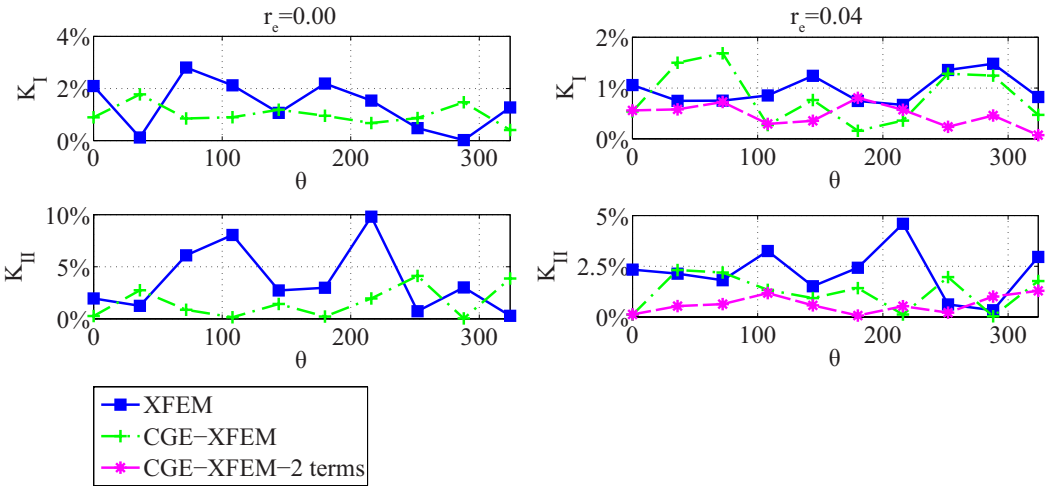

Fig. 24. Lens crack problem. Mode I and II stress intensity factors predicted by XFEM and CGE-XFEM for topological ($r_e = 0.00$ units) and geometrical ($r_e = 0.04$ units) enrichment. The radius of the crack is $R = 0.2$ units and the angle $\alpha = \pi/4$ units, the size of the domain is $L = 1$ unit.

Method	K_I			K_{II}		
	min	max	mean	min	max	mean
XFEM ($r_e = 0.00$)	0.02%	2.80%	1.37%	0.28%	9.81%	3.69%
XFEM ($r_e = 0.04$)	0.67%	1.48%	0.97%	0.33%	4.60%	2.20%
CGE-XFEM ($r_e = 0.00$)	0.40%	1.77%	1.00%	0.03%	4.12%	1.56%
CGE-XFEM ($r_e = 0.04$)	0.16%	1.69%	0.83%	0.03%	2.31%	1.22%
CGE-XFEM-2 terms ($r_e = 0.04$)	0.07%	0.81%	0.47%	0.07%	1.29%	0.61%

Table 3
Lens crack problem. Minimum, maximum and mean values for the errors in the Mode I and II stress intensity factors predicted by XFEM and CGE-XFEM for geometrical ($r_e = 0.04$ units) and topological ($r_e = 0.00$ units) enrichment.

Method	Iterations
XFEM ($r_e = 0.00$)	631
XFEM ($r_e = 0.04$)	16391
CGE-XFEM ($r_e = 0.00$)	282
CGE-XFEM ($r_e = 0.04$)	324
CGE-XFEM-2 terms ($r_e = 0.04$)	416

Table 4
Lens crack problem. Number of iterations required by the solver to solve the system of equations produced by XFEM and CGE-XFEM for geometrical ($r_e = 0.04$ units) and topological ($r_e = 0.00$ units) enrichment. The tolerance of the CG solver was set to 10^{-8}.

pansion in total). In Table 3 the minimum, maximum and mean values of the errors are given while in Table 4 the number of iterations required to solve the resulting systems of equations is given for all the above cases.

The accuracy of the results obtained for standard XFEM is comparable to the one obtained in Moës et al. [5] while the use of geometrical enrichment provides significant reduction (30%-40% in the mean value of the errors). Moreover, the proposed method provides improved accuracy for both topological and geometrical enrichment and can further improve results by employing one higher order term. It is also important to note that the number of iterations to convergence of the conjugate gradient algorithm required for the proposed method for geometrical enrichment is, in every case, smaller even than the number of iterations required by standard XFEM with topological enrichment.

It should be noted that for different values of the distances r_1, r_2 and r_3 or for different meshes (with similar values of the mesh parameter), the behavior of the results can change. In all cases however it is possible to improve the accuracy by employing the proposed method in conjunction to geometrical enrichment and higher order enrichment functions. An important fact regarding the behavior of the results is that for the proposed method the addition of one higher order term provides significant improvement in the results, in fact it provides greater reduction in the errors than the one associated with geometrical enrichment, while the addition of more terms leaves the results almost unaffected.

The above behavior may be explained via the reasoning given in subsection 3.3. An additional problem that arises for curved cracks is the method's inability to account for the change in the orientation of the crack due to lack of spatial variation which might lead to errors. This problem, while being probably negligible when the crack is almost planar inside the enrichment radius, might be more acute for larger enrichment radii and crack curvatures. The use of higher order terms might implicitly help the situation by adding some flexibility, however a proper solution would involve the use of the level set gradients in order to account for the crack curvature as is done in vector enrichment [27].

7 Conclusions

We presented a simple method which shares advantages with both global enrichment introduced in 1973 by [63] and the more recent local partition of unity enrichment of [64,1]. We showed the application of the new approach to three-dimensional linear elastic fracture problems, in particular to non-planar cracks.

The method relies on enrichment within a domain with mesh-independent dimensions within which the enrichment coefficients are constant. Additional variability in the enriched fields is incorporated along the crack front. Novel

numerical integration and stress intensity factor extraction techniques are proposed with particular emphasis on the case where surface tractions are applied.

We achieve optimal convergence and increased accuracy for a fraction of the cost of competing approaches, thanks to the improved condition number of the stiffness matrix.

This containment of the condition number enables the previously difficult or indeed impossible incorporation of higher order enrichment functions.

The method was tested through a series of benchmark problems involving non-planar cracks. These numerical tests indicate:

- An improved accuracy over standard partition of unity enriched finite element methods (up to 50% improvement in the L_2 norm and up to 40% in the energy norm) as well as optimal convergence rates both in the energy and in the L_2 norm for all enrichment domains considered;
- A greatly improved conditioning, which is practically independent of the enrichment radius: the number of iterations to convergence of the conjugate gradient algorithms, for all cases tested, was reduced by 40-50% compared to the variant of the extended finite element method (XFEM) leading to the smallest conditioning number (topological enrichment);
- A simplified implementation which greatly facilitates the extension of the method to higher order finite elements.
- The possibility of using higher order enrichment functions for geometrical enrichment, which had remained impossible due to conditioning issues. These additional functions do lead to improved accuracy in the stress intensity factors.
- For non-planar cracks, a significant improvement (30-40%) in the accuracy of the stress intensity factors and a reduction of the conditioning system matrix. For such non-planar cracks, the effect of the higher-order enrichment functions is much more pronounced.
- The use of geometrical enrichment can substantially improve the accuracy of the predicted stress intensity factors. Moreover, the use of higher order enrichment functions can further improve results while causing a mild deterioration in the conditioning.

One of our long-term goals is the interactive simulation of fracture and cutting [65] and some relevant directions of future work include:

- Modification of the enrichment functions so that the change in orientation is taken into account for non-planar cracks.
- The use of enrichment functions specialized for different types of singularities, for instance enrichment functions that account for the discontinuity occurring when a crack intersects free surfaces. This modification is possible with the proposed method because of the improved conditioning.

- The use of improved integration schemes in order to reduce the computational cost associated with the numerical integration of the enriched part of the approximation.
- The combination of the method with goal oriented a posteriori error estimators [40,41,43,44,45] and local front mesh and FE mesh refinement in order to further improve the accuracy of the method.
- The application of the method to crack propagation problems through the use of different crack representation methods [5,6,50,49,51].
- The reduction of computational expense through reduced order methods such as [66,67,68] or[69,70,71].

Acknowledgements

This work was partially supported by Advanced Research Computing At Cardiff and High Performance Computing (HPC) Wales, a company formed between the Universities and the private sector in Wales which provides the UKs largest distributed supercomputing network.

Eleni Chatzi would like to acknowledge the support of the Swiss National Science Foundation (SNSF) under Research Grant, Project # 200021-153379.

Also Stéphane P. A. Bordas would like to thank partial funding for his time provided by the EPSRC under grant EP/G042705/1 Increased Reliability for Industrially Relevant Automatic Crack Growth Simulation with the eXtended Finite Element Method as well as the European Research Council Starting Independent Research Grant (ERC Stg grant RealTcut, agreement No. 279578) entitled Towards real time multiscale simulation of cutting in non-linear materials with applications to surgical simulation and computer guided surgery.

References

[1] JM Melenk and I Babuska. The partition of unity finite element method: basic theory and applications. *Computer methods in applied mechanics and engineering*, 139(1-4):289–314, 1996.

[2] T Belytschko and T Black. Elastic crack growth in finite elements with minimal remeshing. *International Journal for Numerical Methods in Engineering*, 620(July 1998):601–620, 1999.

[3] N Moës, J Dolbow, and T Belytschko. A finite element method for crack growth without remeshing. *International Journal for Numerical Methods in Engineering*, 46(1):131–150, 1999.

[4] N Sukumar, N Moës, B Moran, and T Belytschko. Extended finite element method for three-dimensional crack modelling. *International Journal for Numerical Methods in Engineering*, 48(November 1999):1549–1570, 2000.

[5] N Moës, A Gravouil, and T Belytschko. Non-planar 3D crack growth by the extended finite element and level sets-Part I: Mechanical model. *International Journal for Numerical Methods in Engineering*, 53(11):2549–2568, April 2002.

[6] A Gravouil, N Moës, and T Belytschko. Non-planar 3D crack growth by the extended finite element and level sets-Part II: Level set update. *International Journal for Numerical Methods in Engineering*, 53(11):2569–2586, April 2002.

[7] SPA Bordas and B Moran. Enriched finite elements and level sets for damage tolerance assessment of complex structures. *Engineering Fracture Mechanics*, 73(9):1176–1201, June 2006.

[8] SPA Bordas, PV Nguyen, C Dunant, A Guidoum, and H Nguyen-Dang. An extended finite element library. *International Journal for Numerical Methods in Engineering*, 71(January):703–732, 2007.

[9] E Wyart, D Coulon, M Duflot, T Pardoen, JF Remacle, and F Lani. A substructured FE-shell/XFE-3D method for crack analysis in thin-walled structures. *International Journal for Numerical Methods in Engineering*, 72(March):757–779, 2007.

[10] E Wyart, M Duflot, D Coulon, P Martiny, T Pardoen, JF Remacle, and F Lani. Substructuring FEXFE approaches applied to three-dimensional crack propagation. *Journal of Computational and Applied Mathematics*, 215(2):626–638, June 2008.

[11] E Wyart, D Coulon, T Pardoen, JF Remacle, and F Lani. Application of the substructured finite element/extended finite element method (S-FE/XFE) to the analysis of cracks in aircraft thin walled structures. *Engineering Fracture Mechanics*, 76(1):44–58, January 2009.

[12] FL Stazi, E Budyn, J Chessa, and T Belytschko. An extended finite element method with higher-order elements for curved cracks. *Computational Mechanics*, 31(1-2):38–48, 2003.

[13] P Laborde, J Pommier, Y Renard, and M Salaün. High-order extended finite element method for cracked domains. *International Journal for Numerical Methods in Engineering*, 64(3):354–381, September 2005.

[14] E Béchet, H Minnebo, N Moës, and B Burgardt. Improved implementation and robustness study of the X-FEM for stress analysis around cracks. *International Journal for Numerical Methods in Engineering*, 64(8):1033–1056, October 2005.

[15] E Chahine and P Laborde. Crack tip enrichment in the XFEM using a cutoff function. *International journal for numerical methods in engineering*, 75(January):629–646, 2008.

[16] A Menk and SPA Bordas. A robust preconditioning technique for the extended finite element method. *International Journal for Numerical Methods in Engineering*, 85(October 2010):1609–1632, 2011.

[17] K Agathos, E Chatzi, SPA Bordas, and D Talaslidis. A well-conditioned and optimally convergent xfem for 3d linear elastic fracture. *International Journal for Numerical Methods in Engineering*, 2015.

[18] I Babuška and U Banerjee. Stable generalized finite element method (sgfem). *Computer Methods in Applied Mechanics and Engineering*, 201:91–111, 2012.

[19] J Chessa, H Wang, and T Belytschko. On the construction of blending elements for local partition of unity enriched finite elements. *International Journal for Numerical Methods in Engineering*, 57(7):1015–1038, June 2003.

[20] TP Fries. A corrected XFEM approximation without problems in blending elements. *International Journal for Numerical Methods in Engineering*, 75(November 2007):503–532, 2008.

[21] R Gracie, H Wang, and T Belytschko. Blending in the extended finite element method by discontinuous Galerkin and assumed strain methods. *International Journal for Numerical Methods in Engineering*, 74(November 2007):1645–1669, 2008.

[22] JE Tarancón, A Vercher, E Giner, and FJ Fuenmayor. Enhanced blending elements for XFEM applied to linear elastic fracture mechanics. *International Journal for Numerical Methods in Engineering*, 77(July 2008):126–148, 2009.

[23] G Ventura, R Gracie, and T Belytschko. Fast integration and weight function blending in the extended finite element method. *International journal for numerical methods in engineering*, 77(July 2008):1–29, 2009.

[24] S Loehnert, DS Mueller-Hoeppe, and P Wriggers. 3D corrected XFEM approach and extension to finite deformation theory. *International Journal for Numerical Methods in Engineering*, 86(October 2010):431–452, 2011.

[25] K Park, JP Pereira, CA Duarte, and GH Paulino. Integration of singular enrichment functions in the generalized/extended finite element method for three-dimensional problems. *International Journal for Numerical Methods in Engineering*, 78(December 2008):1220–1257, 2009.

[26] H Minnebo. Three-dimensional integration strategies of singular functions introduced by the XFEM in the LEFM. *International Journal for Numerical Methods in Engineering*, 92(July):1117–1138, 2012.

[27] N Chevaugeon, N Moës, and H Minnebo. Improved crack tip enrichment functions and integration for crack modeling using the extended finite element method. *Journal for Multiscale Computational Engineering*, 11:597–631, 2013.

[28] G Ventura. On the elimination of quadrature subcells for discontinuous functions in the eXtended Finite-Element Method. *International Journal for Numerical Methods in Engineering*, 66(5):761–795, April 2006.

[29] S Natarajan, SPA Bordas, and DR Mahapatra. Numerical integration over arbitrary polygonal domains based on SchwarzChristoffel conformal mapping. *International Journal for Numerical Methods in Engineering*, 80(July):103–134, 2009.

[30] S Natarajan, DR Mahapatra, and SPA Bordas. Integrating strong and weak discontinuities without integration subcells and example applications in an XFEM/GFEM framework. *International Journal for Numerical Methods in Engineering*, 83(January):269–294, 2010.

[31] SPA Bordas, T Rabczuk, NX Hung, VP Nguyen, S Natarajan, T Bog, NV Hiep, et al. Strain smoothing in fem and xfem. *Computers & structures*, 88(23):1419–1443, 2010.

[32] SE Mousavi and N Sukumar. Generalized Gaussian quadrature rules for discontinuities and crack singularities in the extended finite element method. *Computer Methods in Applied Mechanics and Engineering*, 199(49-52):3237–3249, December 2010.

[33] QZ Xiao and BL Karihaloo. Direct evaluation of accurate coefficients of the linear elastic crack tip asymptotic field. *Fatigue & Fracture of Engineering Materials & Structures*, 26(November 2002):719–729, 2003.

[34] XY Liu, QZ Xiao, and BL Karihaloo. XFEM for direct evaluation of mixed mode SIFs in homogeneous and bi-materials. *International Journal for Numerical Methods in Engineering*, 59(8):1103–1118, February 2004.

[35] A Zamani, R Gracie, and MR Eslami. Cohesive and non-cohesive fracture by higher-order enrichment of XFEM. *International Journal for ...*, 90(January):452–483, 2012.

[36] M Lan, H Waisman, and I Harari. A direct analytical method to extract mixed-mode components of strain energy release rates from irwin's integral using extended finite element method. *International Journal for Numerical Methods in Engineering*, 95(12):1033–1052, 2013.

[37] M Lan, H Waisman, and I Harari. A high-order extended finite element method for extraction of mixed-mode strain energy release rates in arbitrary crack settings based on irwin's integral. *International Journal for Numerical Methods in Engineering*, 96(12):787–812, 2013.

[38] G Song, H Waisman, M Lan, and I Harari. Extraction of stress intensity factors from irwin's integral using high-order xfem on triangular meshes. *International Journal for Numerical Methods in Engineering*, 102(3-4):528–550, 2015.

[39] T Strouboulis, L Zhang, D Wang, and I Babuška. A posteriori error estimation for generalized finite element methods. *Computer Methods in Applied Mechanics and Engineering*, 195(9):852–879, 2006.

[40] SPA Bordas and M Duflot. Derivative recovery and a posteriori error estimate for extended finite elements. *Computer Methods in Applied Mechanics and Engineering*, 196(35-36):3381–3399, July 2007.

[41] M Duflot and SPA Bordas. A posteriori error estimation for extended finite elements by an extended global recovery. *International Journal for Numerical Methods in Engineering*, 76(June):1123–1138, 2008.

[42] S Bordas, M Duflot, and P Le. A simple error estimator for extended finite elements. *Communications in Numerical Methods in Engineering*, 24(11):961–971, 2008.

[43] JJ Ródenas, OA González-Estrada, JE Tarancón, and FJ Fuenmayor. A recovery-type error estimator for the extended finite element method based on singular+ smooth stress field splitting. *International Journal for Numerical Methods in Engineering*, 76(March):545–571, 2008.

[44] JJ Ródenas, OA González-Estrada, P Díez, and FJ Fuenmayor. Accurate recovery-based upper error bounds for the extended finite element framework. *Computer Methods in Applied Mechanics and Engineering*, 199(37-40):2607–2621, August 2010.

[45] OA González-Estrada, JJ Ródenas, SPA Bordas, M Duflot, P Kerfriden, and E Giner. On the role of enrichment and statical admissibility of recovered fields in a posteriori error estimation for enriched finite element methods. *Engineering Computations*, 29(8):814–841, November 2012.

[46] OA González-Estrada, JJ Ródenas, SPA Bordas, E Nadal, P Kerfriden, and FJ Fuenmayor. Locally equilibrated stress recovery for goal oriented error estimation in the extended finite element method. *Computers & Structures*, 152:1–10, 2015.

[47] VF González-Albuixech, E Giner, JE Tarancon, FJ Fuenmayor, and A Gravouil. Convergence of domain integrals for stress intensity factor extraction in 2-d curved cracks problems with the extended finite element method. *International Journal for Numerical Methods in Engineering*, 94(8):740–757, 2013.

[48] VF González-Albuixech, E Giner, JE Tarancón, FJ Fuenmayor, and A Gravouil. Domain integral formulation for 3-D curved and non-planar cracks with the extended finite element method. *Computer Methods in Applied Mechanics and Engineering*, 264:129–144, September 2013.

[49] M Duflot. A study of the representation of cracks with level sets. *International Journal for Numerical Methods in Engineering*, 70(November 2006):1261–1302, 2007.

[50] G Ventura, E Budyn, and T Belytschko. Vector level sets for description of propagating cracks in finite elements. *International Journal for Numerical Methods in Engineering*, 58(10):1571–1592, November 2003.

[51] TP Fries and M Baydoun. Crack propagation with the extended finite element method and a hybrid explicitimplicit crack description. *International Journal for Numerical Methods in Engineering*, 89(November 2011):1527–1558, 2012.

[52] CR Langlois, A Gravouil, MC Baieto, and J Réthoré. Three-dimensional simulation of crack with curved front with direct estimation of stress intensity factors. *International Journal for Numerical Methods in Engineering*, 2014.

[53] J Fish. The s-version of the finite element method. *Computers & Structures*, 43(3):539–547, 1992.

[54] V Gupta, CA Duarte, I Babuška, and U Banerjee. Stable gfem (sgfem): Improved conditioning and accuracy of gfem/xfem for three-dimensional fracture mechanics. *Computer Methods in Applied Mechanics and Engineering*, 289:355–386, 2015.

[55] TP Fries and T Belytschko. The extended/generalized finite element method: an overview of the method and its applications. *International Journal for Numerical Methods in Engineering*, 84(3):253–304, 2010.

[56] MC Walters, GH Paulino, and RH Dodds. Interaction integral procedures for 3-D curved cracks including surface tractions. *Engineering Fracture Mechanics*, 72(11):1635–1663, July 2005.

[57] OC Zienkiewicz, RL Taylor, and JZ Zhu. *The Finite Element Method: its Basis and Fundamentals*. Elsevier, 2013.

[58] Y Renard and J Pommier. Gmm++ library. http://download.gna.org/getfem/html/homepage/gmm/index.html, 2004-2014.

[59] C Geuzaine and J F Remacle. Gmsh: A 3-d finite element mesh generator with built-in pre-and post-processing facilities. *International Journal for Numerical Methods in Engineering*, 79(11):1309–1331, 2009.

[60] ML Kachanov, B Shafiro, and I Tsukrov. *Handbook of elasticity solutions*. 2003.

[61] M Gosz and B Moran. An interaction energy integral method for computation of mixed-mode stress intensity factors along non-planar crack fronts in three dimensions. *Engineering Fracture Mechanics*, 69:299–319, 2002.

[62] MA Martynenko and AF Ulitko. Stress state near the vertex of a spherical notch in an unbounded elastic medium. *International Applied Mechanics*, 14(9):911–918, 1978.

[63] G Strang and GJ Fix. *An analysis of the finite element method*, volume 212. Prentice-Hall Englewood Cliffs, NJ, 1973.

[64] I Babuška, G Caloz, and JE Osborn. Special finite element methods for a class of second order elliptic problems with rough coefficients. *SIAM Journal on Numerical Analysis*, 31(4):945–981, 1994.

[65] H Courtecuisse, J Allard, P Kerfriden, SPA Bordas, S Cotin, and C Duriez. Real-time simulation of contact and cutting of heterogeneous soft-tissues. *Medical image analysis*, 18(2):394–410, 2014.

[66] P Kerfriden, P Gosselet, S Adhikari, and SPA Bordas. Bridging proper orthogonal decomposition methods and augmented newton–krylov algorithms: an adaptive model order reduction for highly nonlinear mechanical problems. *Computer Methods in Applied Mechanics and Engineering*, 200(5):850–866, 2011.

[67] P Kerfriden, JC Passieux, and SPA Bordas. Local/global model order reduction strategy for the simulation of quasi-brittle fracture. *International Journal for Numerical Methods in Engineering*, 89(2):154–179, 2012.

[68] P Kerfriden, O Goury, T Rabczuk, and SPA Bordas. A partitioned model order reduction approach to rationalise computational expenses in nonlinear fracture mechanics. *Computer methods in applied mechanics and engineering*, 256:169–188, 2013.

[69] F Galland, A Gravouil, E Malvesin, and M Rochette. A global model reduction approach for 3d fatigue crack growth with confined plasticity. *Computer Methods in Applied Mechanics and Engineering*, 200(5):699–716, 2011.

[70] S Niroomandi, I Alfaro, D Gonzalez, E Cueto, and Francisco Chinesta. Real-time simulation of surgery by reduced-order modeling and x-fem techniques. *International journal for numerical methods in biomedical engineering*, 28(5):574–588, 2012.

[71] JC Passieux, J Réthoré, A Gravouil, and MC Baietto. Local/global non-intrusive crack propagation simulation using a multigrid x-fem solver. *Computational Mechanics*, 52(6):1381–1393, 2013.